Fracture propagation control in CO_2 pipelines:
Validation of a coupled fluid-structure model

E. Aursand[a], S. Dumoulin[b], M. Hammer[a], H.I. Lange[b], A. Morin[a], S.T. Munkejord[a,*], H.O. Nordhagen[b]

[a]*SINTEF Energy Research, P.O. Box 4671 Sluppen, NO-7465 Trondheim, Norway*
[b]*SINTEF Materials and Chemistry, P.O. Box 4670 Sluppen, NO-7465 Trondheim, Norway*

Abstract

Existing engineering methods to ensure fracture propagation control in natural-gas transmission pipelines have been shown to be non-applicable when dense-phase CO_2 is transported. To overcome this, a coupled fluid-structure interaction model has been developed. It consists of a homogeneous equilibrium flow model, coupled with the Span–Wagner equation of state and including solid-phase formation, and a finite-element model of the pipe taking into account large deformations and fracture propagation through a local fracture criterion.

Model predictions are compared with data from two medium-scale crack-arrest experiments with dense-phase CO_2. Good agreement is observed in fracture length, fracture-propagation velocity and pressure. Simulations show that, compared to natural-gas pipelines, the pressure level at the opening fracture flaps is sustained at a much higher level and at a much longer distance behind the moving fracture tip. This may be one important reason why the existing engineering methods do not work for dense-phase CO_2.

Keywords: Carbon dioxide, Finite-element method (FEM), Computational fluid dynamics (CFD), Fluid-structure, Running-ductile fracture, Pipeline

1. Introduction

According to the Intergovernmental Panel on Climate Change (IPCC) [1], there is 95% certainty that human activity is the dominant cause of observed warming since the mid-20th century. Therefore, climate-change-mitigation efforts must increase. In particular, for the electricity production and industry sector, CO_2 capture, transport and storage (CCS) represents an important and, for many scenarios, a necessary mitigation measure for achieving low-stabilization levels of atmospheric CO_2 [2, 3].

In the two-degree scenario of the International Energy Agency [2], CCS contributes to a CO_2-emission reduction of about 6 Gt per year in 2050. The storage reservoirs will, in general, not be colocated with the capture facilities. Thus, full-scale deployment of CCS will require large amounts of CO_2 to be transported. A large fraction of this is likely to be done by pipelines. For comparison, consider that the Norwegian natural-gas export is about 110 billion standard cubic metres [4], which is roughly 75 Mt per year. Due to the scale alone, it will be of great importance to design and operate CO_2-transport systems in a safe and efficient way. In addition, CO_2 transport will differ from that of natural gas in several ways [see e.g. 5]. The CO_2 will, in most cases, be transported in a liquid or dense liquid state, whereas the natural gas normally is in a dense gaseous state. This affects the behaviour during depressurization, where CO_2 will undergo phase transition. Also, depending on the capture technology, the level and type of impurities will vary [6], and this may significantly alter the thermophysical properties [7, 8, 9].

Several researchers have found that CO_2 pipelines may be more susceptible to long running-ductile fractures (RDF) than e.g. natural-gas pipelines [10, 11, 12, 13]. As a result of this, fracture propagation control (FPC) is an issue that requires careful consideration in the design and operation of CO_2 pipelines. An RDF may be triggered e.g.

---

*Corresponding author.
  Email address: svend.t.munkejord@sintef.no (S.T. Munkejord)

by corrosion or third-party damage to the pipeline. It is governed by the 'race' between the depressurization wave in the fluid inside the pipe, and the fracture-propagation velocity. If the depressurization wave is fastest, the pressure at the fracture tip will decrease and the running fracture will arrest. Otherwise the running fracture may continue for a long distance, causing economical and potentially human loss. It is possible, and indeed required, to design the pipelines to avoid RDF for more than 1–2 pipe sections [14]. For a given operating condition, this may be done by selecting tough enough materials, thick enough pipe walls, or by equipping the pipeline with crack arrestors, which are rings fitted to the exterior of the pipe. All these measures have a cost, and it is therefore of interest to estimate accurately how much is required to maintain safety.

Widespread deployment of CCS will imply that some onshore CO_2-transport pipelines run through or nearby populated areas. Due to the high pipeline pressure and the fact that CO_2 is asphyxiant at high concentrations, safety guidelines and new best-practice manuals will be required. Developing such guidelines demands accurate models for predicting both the risk and evolution of pipeline fractures [15]. Pipelines can then be designed specifically to avoid the significant hazards and financial costs associated with the formation of a long RDF – while reducing the need for safety factors.

1.1. Existing FPC methods for pipelines

Several approaches to predict and understand the RDF problem in pipelines, and thus obtain FPC in pipelines, have been developed over the years (see [16, 17, 18] for a more complete review). These approaches to FPC in pipelines can be divided into three classes:

Class 1: semi-empirical methods based on correlations with full-scale experiments e.g. [19, 20, 21],

Class 2: energy-balance-based methods e.g. [22, 23] and

Class 3: direct (fluid-structure interaction) calculations e.g. [10, 24, 25, 26, 27, 28].

The first two classes consider the fluid and the structure to be uncoupled, and the resulting computations are not intensive. The energy-based approaches are not widely used for engineering purposes, but might e.g. give important insight into the relative importance of different parameters in the RDF problem, e.g., as done in [22, 23]. In the third class of approaches, the fluid and the structure are more or less coupled, and the resulting computations are much more intensive, though in most versions, the fluid-mechanics calculations do not consider the interaction between the opening fracture flaps and the fluid flow.

The engineering methods, represented by the first class above, are the main tool used for handling FPC and RDF problems in pipelines today. These are semi-empirical and have been developed mainly for natural-gas transport and for older steel types [29]. Such models need (at best) re-calibration when applied to CO_2-transporting pipelines or more modern-type high-strength pipeline steels [29, 30]. In fact, all classes of approaches suffer from a combination of the following issues, especially when applied to high-strength and high-toughness steels or dense-phase CO_2 or CO_2-mixtures is being conveyed:

- **Estimation of dynamic fracture toughness**: Impact tests (e.g. the Charpy test) have traditionally been linked directly to the ability of the material to resist dynamic ductile crack growth (all Class 1 methods). For modern high-toughness steels, the correlation of impact energy to the fracture velocity and the arrest pressure becomes questionable, and the fracture resistance seems to be more dependent on the plastic flow properties of the steel [16]. Among most Class 3 approaches, impact tests [10, 27] and similar tests [31] measuring the crack tip opening angle are also used [24] to evaluate the dynamic fracture resistance. In [25] and [26] a more physically-based elastic-plastic material description is used and cohesive zone elements are used to represent the dynamic fracture.

- **Fluid mechanics of two-phase decompression**: To obtain a physical description of RDF, it is essential to describe the spatially and temporally varying load on the pipe. Herein, a boiling two-phase fluid will sustain a higher pressure than a single-phase fluid. In the semi-empirical Class 1 approach, it is assumed that the fluid is in equilibrium, and it is implicitly assumed that the pressure profile, and hence the load profile on the pipe (even where the crack is open), does not substantially change from the conditions at which the experiments were carried out. In Class 3 approaches, simplifications are also made. In [25], a pressure profile is prescribed, while

in [10], the fluid pressure is calculated based on computational fluid dynamics (CFD), but only the pressure at the crack-tip position is assumed to influence the fracture velocity.

- **Computationally demanding**: The Class 3 approaches, except the model in [27], require long computation times as they either rely on heavy 3D CFD computations [24], many-particle simulations [26], or rich structural finite-element meshes [25]. For the Class 3 approaches to serve as an alternative or complementary approach to the Class 1 approaches, computational efficiency is essential.

All existing approaches to RDF contain at least two of the issues listed above. One may therefore state that there is no existing efficient methodology for calculating the material parameters or pipe-wall thickness appropriate for arresting a propagating ductile fracture in a pipeline transporting dense-phase CO_2.

The objective of this work is to present a numerical methodology for FPC aiming to include the important physics and to be tractable for a desktop computer. In this way, a tool for safe and cost-effective design and operation of CO_2 pipelines can be established. The methodology comprises two main parts: a one-dimensional CFD model accounting for the fluid flow inside, and out of, the pipe, and a structure-mechanics model using the finite-element method (FEM) accounting for the non-linear mechanical behaviour of the pipe wall and employing a local stress-based fracture criterion. A two-way coupling between these two parts is implemented. This coupled fluid-structure model has been validated against crack-arrest experiments performed with methane and hydrogen [15, 32], and it has later been extended to accurately account for two-phase (gas-liquid) and three-phase (gas-liquid-solid) CO_2 [13, 33, 34, 35]. In the present work, the model is extended with an improved method to estimate the circumferentially varying pressure load on the fracture flaps, and a backfill model is employed to represent the material surrounding the pipe.

Recently, several research programmes have been initiated to prepare the industry for CCS and address the issue of FPC in CO_2 pipelines. The COOLTRANS project, run by National Grid (UK) has carried out and published results from five experiments connected to FPC in dense-phase CO_2 pipelines [11, 36]. Two of these were full-scale crack-arrest experiments with a CO_2-N_2 mixture, and the conclusion was that the common method to address the FPC issue in pipelines, the Battelle Two Curve Method (BTCM) [20], 'is grossly non-conservative' [11] and 'not (currently) applicable to liquid or dense phase CO_2 or CO_2-rich mixtures' [12].

In the joint industry project CO2PIPETRANS, run by DNV-GL, a number of significant gaps in knowledge – in particular related to FPC – were identified in the recommended practice [37]. Two medium-scale crack-arrest experiments were performed in 2012 with dense-phase CO_2, and these results will be employed to validate the present fully coupled fluid-structure model. To our knowledge, this is the first time a coupled fluid-structure model has been validated with crack-arrest data for a CO_2 pipeline.

The rest of this paper is organized as follows: The crack-arrest experiments are described in Section 2, while Section 3 presents the coupled fluid-structure model. Section 4 describes how backfill is accounted for. All results are given in Section 5 and discussed in Section 6 before conclusions are drawn in Section 7. Appendix A presents the two-curve methods which we employ for reference.

2. The crack-arrest experiments

Two medium-scale crack-arrest experiments, identified as Test 1 and Test 2, with the original aim of evaluating the applicability of the BTCM for determining ductile crack arrest in dense-phase CO_2-transporting pipelines, were performed in the CO2PIPETRANS project [38]. The results from these experiments are employed here to validate our coupled fluid-structure methodology. In the following, some details about the two tests are presented.

2.1. Test layout

Four different types and thicknesses of steel pipeline stokes were used in each test – each with a length of approximately 5.5 m and with an outer diameter of about 16 inch, i.e. 406 mm (see Figure 1). The pipe stokes W1 and E1 were the pipes where ductile fracture was supposed to propagate and arrest. The two outer stokes (W2 and E2) were acting as gas reservoirs and intended to ensure crack arrest in case the fracture would travel through the test pipes, and provide sufficient length to avoid the reflecting pressure wave to interfere with the propagating fracture. Approximately the same pipe-stoke geometries and test layout were used in the two tests. All pipe stokes were High Frequency Induction (HFI) welded pipes, except the 12.7 mm E2 pipe which was seamless (SMLS). All pipe stokes were of type

3
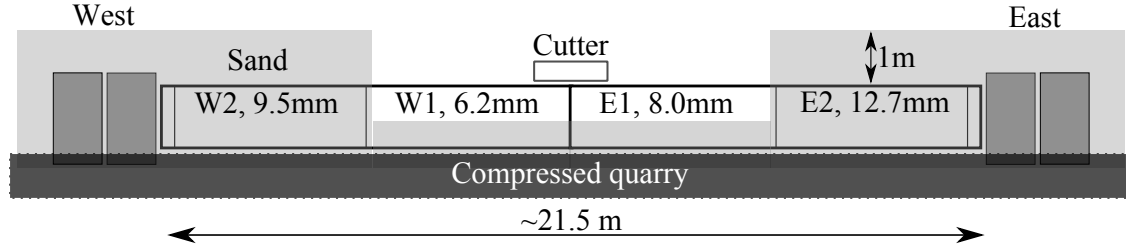
Figure 1: Layout of tests, with pipe thickness denoted after the pipe stoke definitions (W2, W1, E1, E2). The outermost concrete blocks are only present in Test 2. Grey and dark opaque shades indicate the sand backfill and the compacted quarry plate, respectively. The 800 mm directed explosive cutter is also illustrated.

Table 1: Pipe material, thickness and length used in the two tests.

Test No./Pipe		W2	W1	E1	E2
Material		X60	L415MB	X65 M	L450Q
Test 1	Mean diameter (mm)	396.92	403.62	398.82	396.40
	Thickness (mm)	9.52	6.22	7.82	13.0
	Length (mm)	5560	5485	5565	4785
Test 2	Mean diameter (mm)	397.0	401.0	398.29	393.98
	Thickness (mm)	9.60	6.10	7.79	12.88
	Length (mm)	5562	5568	5565	4780

C-Mn steel. A 60 mm thick 420 C-Mn steel plate was welded onto the open ends of the reservoir pipes (W2 and E2). The position of the longitudinal seam welds were positioned between the 5 and 7 o'clock positions (with 12 o'clock being the expected fracture path) – with a slight rotation between the pipes to avoid line-up of the welds. All pipe stokes had a similar outer diameter from 406 to 410 mm, but varying inner diameter due to different wall thickness (see Table 1). Reported wall thickness were measured at several positions along the pipes and averaged. The total pipe length of each of the two experiments was 21.5 m.

At the test site, the pipes were positioned on a laser levelled compressed quarry plate. Concrete blocks were positioned at each end of the set-up to restrict horizontal movement. Their weight was increased from 3.5 tonnes each in Test 1, to 7 tonnes in Test 2. The reservoir pipes (W2 and E2) had a 1 m sand backfill on top. Loosely compacted sand backfill up to a height of a half pipe diameter and width of approximately 0.5 m, was used on the test pipes (W1 and E1).

2.2. Materials

All pipe materials were mechanically characterized using a traditional Charpy impact test (ISO 148-1) and tensile test (ISO 6892-1). The respective values for the 0.2 % offset yield strength, σ_0, the ultimate tensile strength, σ_{TS} and the Charpy energy (CVP) at room temperature, and with specimen orientation in transverse direction, for the various pipe stokes in the two experiments, are given in Table 2. An equivalent 80 mm^2 cross-section specimen was used for calculation of CVP. Results from Charpy impact tests showed high Charpy energy values (CVP > 100 J) at temperatures relevant for the testing conditions – indicating that ductile fracture behaviour during testing was to be expected. Flattened full-thickness test specimens (type DIN 50125), taken in both the rolling direction (Long) and the transverse (Trans) direction, were used for the tensile properties reported in Table 2. Additional tensile tests were performed on non-flattened cylindrical specimens taken from the mid-section of the test stokes (W1 and E1). This was necessary for calibration of material and fracture models used in the coupled model. This will be further discussed in Section 3.1.

4

Table 2: Pipe materials used in Test 1 (left) and Test 2 (right). The 0.2 % offset yield stress, σ_0, tensile strength, σ_{TS}, and the full-size-equivalent Charpy energy, CVP, were taken from full-thickness flattened specimens at room temperature. Charpy cross section specimen dimensions for ligament was $8.0\,\mathrm{mm} \times 7.5\,\mathrm{mm}$ for E1 and W2, $8.0\,\mathrm{mm} \times 5.0\,\mathrm{mm}$ for W1 and full size for E2.

Test 1					Test 2				
Pipe	Direction	σ_0 (MPa)	σ_{TS} (MPa)	CVP (J)	Pipe	Direction	σ_0 (MPa)	σ_{TS} (MPa)	CVP (J)
W2	Long	508	568		W2	Long	494	558	
	Trans	449	557	231		Trans	458	564	241
W1	Long	445	570		W1	Long	454	578	
	Trans	430	584	128		Trans	421	583	121
E1	Long	344	469		E1	Long	332	467	
	Trans	299	463	154		Trans	299	467	144
E2	Long	532	619	367	E2	Long	498	587	328

2.3. Instrumentation

The two tests were instrumented with pressure transducers (Kulite XTL-190M), internal temperature probes (K thermocouples) and timing wires. A shaped charge with length 800 mm and positioned on the centre girth weld in the axial direction, was used to create the initial fracture in the pipe. The calibrated pressure transducers, connected to the pipe with a weldolet, were levelled with the internal surface of the pipes, and placed at the 3 o'clock position at 1, 3 and 5 m on each side of the centre girth weld. Timing wires were mounted symmetrically, starting 100 mm from the ends of the initial crack. The timing wires were made of 10 mm wide strips and 0.1 mm thick high-strength brass with a fracture strain of 2–3%. A spacing of 250 mm and 500 mm was used for the first 5 and 10 following timing wires, respectively. The timing wires were attached to the pipe using Araldite adhesive type 2015. A base layer of Araldite was first made to electrically insulate the strip from the steel. The strip was glued onto the base layer. In order to measure the arrival of the fracture at the timing wire, resistors were connected between the parallel connected timing wires. Amplification of the pressure transducer signal was done with an in-house designed high-speed DC amplifier, and logging was performed with National Instrument PCI 6133 cards connected to a PC. A logging frequency of 1 MHz was used during the tests. The 800 mm initiation crack was made using a shaped charge (Diaplex 30 frame), packed evenly with C4 explosive to an extent of $290\,\mathrm{g\,m^{-1}}$, based on pre-trials. The initial crack width caused by the shaped charge in the W1 pipes is not known, but most likely it would be in excess of 10 mm. A cutting time of 0.05 ms for the 800 mm crack was measured in pre-trials. This time delay was added to the reported pressure and timing wire measurements.

2.4. Test conditions

The aim of the two tests was to check whether FPC based on BTCM predictions agreed with the experiments. Therefore, two initial states for the CO_2 were sought; one where no-arrest was predicted (Test 1), and one where crack arrest was predicted in the test pipes (Test 2). This was achieved by adjusting the initial temperature such that, upon depressurization, the CO_2 would hit the two-phase region at the desired saturation pressure. The arrest versus no-arrest boundary was calculated based on the BTCM described in Appendix A.1. Due to the increase of the saturation pressure with increasing initial temperature, T_i, and decreasing initial pressure, p_i, Test 1 was run at a higher initial temperature and a (slightly) lower initial pressure than Test 2 (see Table 3). In the two experiments, the temperature was manually controlled by heating mats covering the pipes, and by numerous thermocouples measuring the temperature in the steel and in the fluid. Ample time for temperature stabilization of the fluid was allowed in both tests.

2.5. Results from the two crack-arrest tests

A summary of the test conditions and results from the two tests can be found in Table 3. Pictures from the two crack-arrest tests can be seen in Figure 2. The experiments agree with the BTCM predictions in the sense that the running fracture was arrested in Test 2, but not in Test 1. In both Test 1 and Test 2, the fractures propagated as a through-thickness slant fracture, and arrested through a ring-off mechanism in the reservoir girth welds and test pipes, respectively. Details on the pressure recordings and fracture velocities from the two tests will be reported in Section 5.

Table 3: Initial experimental conditions and results from the two tests. Final crack length (Cr.length) and average velocity includes only the parts of the fracture from the tip of initial fracture and until arrest through deviation from a straight fracture (i.e. through ring-off). The given saturation pressure, p_{sat}, is for the isentrope from the initial state, as calculated from the Span–Wagner equation of state. The experimental fracture velocity, v_f, and the time of crack arrest, t_a, are estimated.

Test	p_i (bar)	T_i (°C)	p_{sat} (bar)	Pipe Stoke	Avg. v_f (m s^{-1})	Cr.length (m)	t_a (ms)
Test 1	88.5	30.0	64.0	West 1	185	5.08	27.5
				East 1	135	5.16	34.4
Test 2	91.5	8.6	38.6	West 1	118	1.4	21.7
				East 1	78	1.0	29.8

2.5.1. Test 1

In Test 1, the RDF in both east and west directions propagated through the test pipes (W1 and E1) and arrested at the welds to the W2 and E2 pipes (branching along the girth weld), respectively. Due to post test shaking of the ground in Test 1, the high-speed PCI card registering the timing-wire data loosened, and the timing wire data were lost. Fracture velocities from Test 1 were therefore calculated from the high-speed video recording and the sudden drop in the pressure sensors upon passing of the RDF. Average fracture velocities, v_f, reported in Table 3, are estimated up to 4 m of fracture propagation. The time elapsed between detonation of the explosive cutter and crack arrest, t_a, is estimated based on the average velocity – and is therefore quite uncertain. A complete separation of the pipes W2 and W1, and an almost complete separation between E2 and E1, happened upon crack arrest in Test 1 (see Figure 2a). During the test, the 3.5 tonne concrete blocks supporting the ends were pushed several metres away, the W2 pipe was ejected about 40 m in the axial direction and the remaining pipes (E1, E2 and W1) displaced sideways about 4 m.

2.5.2. Test 2

From the experience in Test 1, it was decided to double the weight of the end blocks in Test 2, as well as to place two similar blocks on top of the girth welds (placed on pillars so as not to come in contact with the pipe) between W1/W2 and E1/E2. In Test 2, the running fracture in W1 and E1 started to deviate from the 12 o'clock position after about 1.4 and 1.0 m of propagation from the tip of the initial fracture, respectively (see Figure 2b). That is, both the fractures running in opposite directions in Test 2, arrested through a ring-off mechanism, and propagated an additional 100–150 mm in the axial direction following the ring-off initiation. The reported measured crack lengths only include the part of the fracture travelling in the straight axial direction after the initial crack was established, and before initiation of ring-off. As for Test 1, there is some uncertainty in the estimated crack-arrest time, t_a.

3. The coupled model

This section describes the coupled fluid-structure interaction model addressing fracture propagation control (FPC) in CO_2 pipelines. Through advanced modelling of the fluid- and thermodynamics of CO_2 and the structural and material response resulting from a direct coupling, we aim to describe running-ductile fracture (RDF) in CO_2 pipelines in a physically sound and computationally efficient way.

The coupled model consists of two main parts: a structure model accounting for the steel pipeline with a fracture and the surrounding material (backfill), and a fluid-dynamic model accounting for the fluid behaviour. The structure model passes the fracture opening and pipe geometry to the fluid-dynamic model, which then calculates the flow through the fracture and the pressure field along the pipe axis. Next, this pressure field is passed to the structural model and applied onto the finite elements. Each part of the coupled model will be described in the following.

3.1. Structure model

The pipeline structure has been modelled using the finite-element (FE) code LS-DYNA [39]. The deformation and fracture of the pipe have been modelled using shell elements and an elasto-visco-plastic constitutive equation [15] with a local ductile fracture criterion [40] previously developed (e.g. [41], [42]). These are implemented in LS-DYNA through a user material subroutine. The simulations consisted of two stages: first, the pipe was loaded to the initial pressure using an implicit scheme, followed by the RDF using an explicit scheme. Although pipeline

(a) Test 1.

(b) Test 2.

Figure 2: Pictures from the two tests. The red arrow in the left picture indicates the position of girth weld between W1 and E1 pipe stokes.

materials often show a certain degree of plastic anisotropy, strain-rate sensitivity and thermal softening, we have for simplicity described the material using an isotropic yield criterion (von Mises) and a viscoplastic non-linear isotropic work-hardening rule (Voce-like) including a linear dependence of the yield stress on temperature.

3.1.1. The isotropic elasto-plastic constitutive equations

The yield function, f, which defines the elastic domain in stress space, is expressed in the form

$$f(\boldsymbol{\sigma}, \epsilon_{\mathrm{p}}) = \sigma_{eq}(\boldsymbol{\sigma}) - (\sigma_0 + R(\epsilon_{\mathrm{p}})) \left(1 + \frac{\dot{\epsilon}_{\mathrm{p}}}{\dot{\epsilon}_{\mathrm{P}0}}\right)^C \left(1 - \left(\frac{T - T_r}{T_m - T_r}\right)\right)^m, \tag{1}$$

where $\boldsymbol{\sigma}$ is the stress tensor, σ_{eq} is the von Mises equivalent stress, σ_0 is the yield stress in the reference direction, $R(\epsilon_{\mathrm{p}})$ is the isotropic hardening variable, $\dot{\epsilon}_{\mathrm{p}}$ is the equivalent plastic strain rate, ϵ_{p} is the equivalent, or accumulated, plastic strain, $\dot{\epsilon}_{\mathrm{P}0}$ is the reference strain rate, C is the instantaneous rate sensitivity of the flow stress, T is the material temperature, T_m is the melting temperature (1800 K), T_r is the reference temperature (at which σ_0 is defined) – here room temperature – and m controls the temperature sensitivity of the yield stress. The elastic modulus, E, and Poisson ratio, ν, are assumed to have a constant value of 208 GPa and 0.3, respectively.

The isotropic work-hardening rule is defined using a two-term Voce equation [43]

$$R(\epsilon_{\mathrm{p}}) = \sum_{i=1}^{2} Q_i \left(1 - \exp\left(-\frac{\theta_i}{Q_i} \epsilon_{\mathrm{p}}\right)\right), \tag{2}$$

where θ_i and Q_i are the initial hardening moduli and the saturation values, respectively, for each term.

3.1.2. The fracture model

From the perspective of material modelling, the greatest obstacle to simulate an RDF, is the lack of a complete understanding of the physical mechanisms governing the phenomenon (see e.g. [44]). The fracture has a velocity in the axial direction of the pipe of about 100–300 m s^{-1}, and typically propagates as a through-thickness slant fracture. That is, the fracture surface forms a close to 45° angle with the pipe surface – sometimes with a dynamic transition between different modes [45]. This fracture appearance is not specific for dynamic ductile fractures, but appears in general in situations with approximately plane-strain conditions in the preferred crack-propagation direction. Although the exact physical mechanisms leading to the final slant fracture can be considered as unknown, it is likely

7

that a through-thickness localization of plastic strain occurs in the neck ahead of the propagating fracture and might trigger the final surface separation. Through a combination of plastic strain localization [46], void-sheeting [47] and (in case of dynamic fracture) adiabatic heating, free fracture surfaces are generated. However, in the literature, there are indications that capturing the exact mechanisms leading to the slant fracture is not necessary to achieve a good engineering representation and prediction of the fracture resistance [25, 48]. In this paper, a simplified approach is used to describe fracture. The fracture model assumes that damage evolution (e.g. void growth) does not influence the material behaviour, i.e., there is no softening of the material prior to fracture. Fracture propagation is described by element erosion when the Cockcroft-Latham (CL) ductile-fracture criterion [40] is fulfilled in one integration point. The CL fracture criterion states that fracture occurs when the tensile principal stress integrated over the strain path reaches a critical value

$$W = \int_0^{\epsilon_e} \langle \sigma_I \rangle \mathrm{d}\epsilon_e \leq W_c, \ \langle \sigma_I \rangle = \max(\sigma_I, 0). \tag{3}$$

Here σ_I is the major principal stress, ϵ_e is the strain at fracture and W_c is a material constant that should be determined from a suitable experiment, typically a tensile test. We have here assumed that W_c does not depend on the plastic strain rate, $\dot{\epsilon}_\mathrm{p}$ (see e.g. [49]).

Though only one free parameter is used in calibrating the fracture criterion, it can be shown that Eq.(3) depends on both the stress triaxiality (ratio of mean stress to effective stress), Lode parameter (the third stress invariant) and plastic straining.

3.1.3. Calibration of material model for test pipelines

There are altogether 9 material parameters that must be calibrated: 4 for the work-hardening rule (Eq. (2)), 1 for the fracture model (Eq. (3)), and 4 parameters for the yield stress, strain rate and temperature sensitivity (Eq. (1)). The parameters characterizing the temperature and strain-rate sensitivity were taken from the literature (see below), and the rest were calibrated using quasi-static uniaxial tensile tests.

Though tests on flattened specimens in Table 2 show some variation between the E1 and W1 test pipes in Test 1 and Test 2, insignificant variations were observed in the measured stress-strain curves from the cylindrical specimens. Thus, it was assumed that E1 and W1 materials did not vary between Test 1 and Test 2. Therefore, only the materials for the W1 and E1 pipe stokes were characterized and all material properties (except the thickness) were assumed equal in E1 and E2, and in W1 and W2.

Tensile tests were performed on smooth axisymmetric specimens oriented in both the longitudinal (reference direction) and transverse direction of the pipe. The specimens had a parallel gage length of 6 and 4.5 mm and a cross-sectional diameter of 3 and 4 mm, for each of the W1 and E1 pipe stokes, respectively. The tests were performed at room temperature and at an average strain-rate of $10^{-3}\,\mathrm{s}^{-1}$. Three tests were performed for each direction. The force and minimum cross-section area of the specimens were continuously monitored until fracture. This was done using a purpose-built measurement rig where two perpendicular lasers accurately measured the minimum specimen diameters (see description of the method in e.g. [50, 51]). The resulting stress-strain curves for each material showed excellent repeatability, but with some scatter in the strain at fracture. Except for a slightly lower fracture strain in the transverse direction, the materials showed almost in-plane isotropic elastic-plastic properties while out-of-plane anisotropy was observed. However, a previous numerical study showed that anisotropy does not affect RDF [52]. The materials were therefore considered isotropic. One representative curve for each material (W1 from Test 1 and E1 from Test 2) was chosen among the tests oriented in the longitudinal direction. The model parameters for the work-hardening rule were calibrated with the design optimization tool LS-OPT [53] against the experimental engineering stress-strain curves. The fracture parameter W_c was then determined manually, by trial and error, within 3 trials. A comparison of the experimental and numerical true stress versus true strain curves is shown in Figure 3, where an excellent agreement is observed.

In the absence of data, the strain-rate sensitivity was assumed to be the same for both materials and similar to an X65 pipeline steel calibrated earlier [15]. Thus, the parameters representing strain-rate sensitivity, $\dot{p}_0$ and C in Eq. (2), were taken from [15]. Similarly, even though the yield stress may exhibit a non-linear relationship with temperature (e.g. [54]), a linear dependence is assumed here as often adopted in the literature (e.g. [41], [55]). All material parameters calibrated for the test pipes are given in Table 4. In the simulations, the steel temperature was assumed to be constant and equal to the initial temperature of the experiment, except for one case, where thermoplasticity was considered.

8
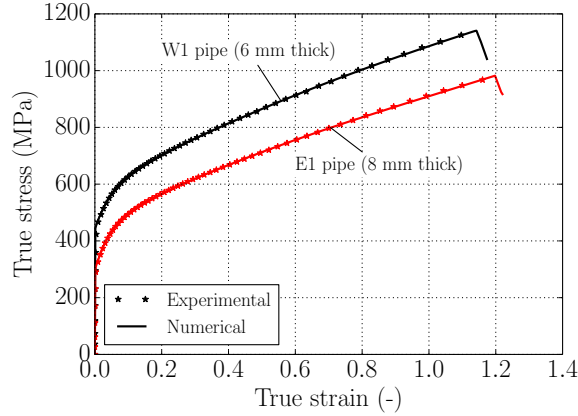
Figure 3: Comparison of true stress versus true strain curves from experiments and modelling for the W1 and E1 materials.

Table 4: Material parameters for the structure model (in the longitudinal direction) used in the finite element model. No thermoplastic effects were considered (i.e. $T = T_r$) except in the results presented in Figure 13a, where the values $T_i = 286.6$ K, $T_r = 300$ K, $T_m = 1800$ K, $m = 1.0$ found in the literature were used.

	σ_0 (MPa)	θ_1 (MPa)	Q_1 (MPa)	θ_2 (MPa)	Q_2 (MPa)	W_c (MPa)	$\dot{p}_0$	C	m
W1	446.1	3184.2	140.7	657.2	350.7	1240.0	0.015	0.011	1.0
E1	302.3	3610.8	145.3	716.1	339.9	1010.0	0.015	0.011	1.0

3.1.4. The FE spatial discretization

As discussed in [48], a neck will be travelling in front of an RDF – with a correspondingly large area of plastic thinning of the pipe material. This energy uptake will account for most of the work done by the escaping gas [22, 23]. Although the specific fracture energy is orders of magnitude less than the total work [22, 23, 48] done by the fluid on the pipe, the fracture criterion controls the extension and amount of thinning of the pipe during the RDF – and therefore also the fracture velocity.

In fracture mechanics, computational cells are used to introduce a physical length-scale into the FE model over which continuum damage occurs. Computational cells are FEs in the process zone having their characteristic size determined by the physical process under consideration [56]. A similar route may be taken to describe plastic failure in the steel pipeline when using shell elements, i.e., the characteristic element length is determined by the length scale of the phenomenon responsible for failure, local necking. For shell elements the width of the local neck is independent of the thickness and typically equal to the width of the elements. Hence, localized necking becomes mesh dependent. However, if we assume that the length scale of local necking, i.e., the width of the local neck, is about the pipeline thickness, it is reasonable to expect that a mesh with characteristic element size approximately equal to the sheet thickness would give good results. For the results presented in this paper, the initial characteristic size of the elements where fracture is expected to occur was about 7.5 mm. To ensure an element aspect ratio at failure close to one, the elements located at the expected fracture path had a length of 15 mm in the pipe axial direction. The remaining elements in the pipe had element edge lengths of approximately 15 mm. All elements in the shell model had the same fracture criterion and fracture parameter, but due to the chosen initial aspect ratio of the top annular elements, a slight preference for a straightly propagating crack was made. The Belytschko-Tsay element formulation, with one in-plane integration point and five integration points through the thickness, was used.

3.2. Fluid model

Following our earlier work [13, 35], we model the one-dimensional compressible flow of pure CO_2 using the homogeneous equilibrium model and the Span–Wagner [57] reference equation of state (EOS). The flow model may

9

be written as

$$\frac{\partial \rho}{\partial t} + \frac{\partial (\rho u)}{\partial x} = -\zeta$$

$$\frac{\partial (\rho u)}{\partial t} + \frac{\partial (\rho u^2)}{\partial x} = -u_{x,e}\zeta \tag{4}$$

$$\frac{\partial E}{\partial t} + \frac{\partial ([E + p] u)}{\partial x} = -\left(h_e + \frac{1}{2}u_e^2\right)\zeta,$$

where on the left-hand side, x is the axial position, t is the time, ρ is the density, u is the velocity in the axial direction, E is the total energy per volume, and p is the pressure. The quantity E can be written as

$$E = \rho\left(e + \frac{1}{2}u^2\right), \tag{5}$$

where e is the specific internal energy. The quantity $h = e + p/\rho$ is the specific enthalpy. The right-hand-side terms are source terms accounting for the local exchange of mass, x-momentum and energy, through the fracture opening. The details of these terms are shown in Section 3.2.1.

For each set of local (ρ, E) obtained from the flow equations (4), a density–energy flash routine [33] using the Span–Wagner EOS is used to find the corresponding local equilibrium state, providing variables such as pressure, temperature, the number of phases present, the densities of each phase, and the volume fraction of each phase. The possible formation of dry ice is accounted for combining the Span–Wagner EOS with a correlation for the sublimation line, $P_{subl} = P_{subl}(T)$, the Clapeyron equation, and an empirical polynomial for $\rho_s(T)$ [34]. For single-phase flow, the above formulation (4) reduces to the Euler equations. For multiphase flow, it is applicable if one assumes that there is no velocity difference (slip) between the phases. For such flows, the model is often referred to as the homogeneous equilibrium model (HEM). The relationships between the variables of the homogeneous equilibrium model (4) and the quantities of the individual phases are

$$u = u_g = u_\ell = u_s$$

$$\rho = \alpha_g\rho_g + \alpha_\ell\rho_\ell + \alpha_s\rho_s \tag{6}$$

$$E = \alpha_g\rho_g\left(e_g + u^2/2\right) + \alpha_\ell\rho_\ell\left(e_\ell + u^2/2\right) + \alpha_s\rho_s\left(e_s + u^2/2\right),$$

where g, ℓ and s denote gas, liquid and solid, respectively. Herein, α_k is the volume fraction of phase k.

3.2.1. Source terms

The source terms on the right-hand side of Eq. (4) were derived by enforcing conservation of mass, x-momentum and energy in each computational cell, given fluxes along the pipeline axis and the fracture opening. To arrive at the form in Eq. (4), it is assumed that most of the momentum in the pipeline is x-directed when considering the entire cross section. The fluxes through the fracture opening generally depend on the local fluid state at the escape point, where the quantities are designated by subscript e. They are different from the averaged quantities, which are evolved by Eq. (4) and represent the state of the local pipeline cross section as a whole, and are written with no subscript. Figure 4 illustrates the outflow model, and how the averaged quantities relate to the escape quantities.

The factor ζ is the rate of mass loss per volume, given by

$$\zeta = \rho_e u_{y,e}\frac{A_e}{V_{cell}}, \tag{7}$$

where in the fraction, A_e represents the local size of the fracture opening compared to the local pipeline volume, V_{cell}.

What remains in order to know the source terms in Eq. (4) is to find the escape quantities given the corresponding averaged quantities in the pipeline. This is done by considering compressible quasi-steady Bernoulli flow along a streamline from the pipeline interior to the escape point, as illustrated in Figure 4. Along such a streamline, we know that

$$\frac{1}{2}u_s^2 + h_s = C \quad \text{(Constant along streamline)}, \tag{8}$$

10
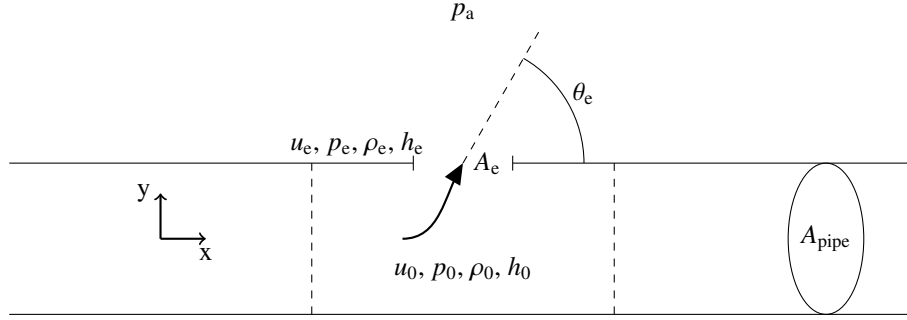
Figure 4: Illustration of the leakage from the pipeline through a radial opening. The leakage model assumes isentropic quasi-steady outflow from a homogeneous state inside the pipeline given by pressure p_0, mixture density ρ_0 and mixture specific enthalpy h_0. A leakage streamline is imagined, starting from this state inside the pipeline, and ending at an angle of θ_e at the entry point of an opening of area A_e. The state at this point is designated by subscript e. The ambient pressure, outside the valve, is given by p_a.

where u_s is the velocity along the streamline, and h_s is the specific enthalpy along the streamline. The initial state of this streamline corresponds to the averaged pipeline state, with u_s equal to the local axial velocity u_0. The final state of this streamline is the needed escape state, meeting the escape surface with a speed u_e at an angle θ_e.

Just like inside the pipeline in general, it is assumed that the fluid maintains instantaneous local thermodynamic equilibrium along the streamline. Further, the outflow streamline is assumed to be isentropic, since the outflow is so rapid that the effects of friction and external heat transfer have a negligible effect on the flow behaviour. (See discussion in e.g. [58].)

The reason that the escape pressure is not always simply the ambient pressure, p_a, is the phenomenon of *choked flow*, which sets a limit on how fast a fluid may flow from high to low pressure through an opening, and thus also sets a limit on how low the pressure can become in this opening. Because the flow is assumed to be steady and adiabatic, we may employ a simple form of choked flow theory, which states that the escape velocity cannot exceed the local speed of sound at the point of escape, i.e.

$$u_e \leq c_e, \tag{9}$$

when we assume that the narrowest flow cross section is at the escape point. When Eq. (9) is satisfied as an equality, the outflow is said to be choked.

The equation of state gives the ability to calculate the specific enthalpy, h, and the local speed of sound, c, given a pressure, p, and a specific entropy, s. One may then search for the pressure which solves the choke condition

$$u(p, s_0) = c(p, s_0), \tag{10}$$

where

$$u(p, s_0) = \sqrt{2\left[h_0 - h(p, s_0)\right] + u_0^2}. \tag{11}$$

Here, s_0 and $h_0(p_0, s_0)$ are the specific entropy and specific enthalpy of the initial state of the streamline. Note that according to the isentropic assumption, $s = s_0$ along the entire streamline, while h is allowed to change from its initial value of h_0. Isentropes (lines of constant s) starting in the dense-phase area, at temperatures and pressures relevant for pipeline transport, will meet the saturation (two-phase) line, and continue following it towards the triple point. The goal is to identify the pressure level along the s_0 isentrope where Eq. (10) is satisfied. Special care must be taken with the fact that the equilibrium speed of sound, $c(p, s_0)$, is a discontinuous function of pressure when meeting the saturation line. If the outflow speed is within the range of the jump in c at this point, this is interpreted as choke at entry into the two-phase region.

The above is a search for what the choke pressure would be, given that the ambient pressure is low enough to induce choking. This is independent of what the outside ambient pressure actually is. Of course, if the choke pressure found from the above procedure is lower than the actual ambient pressure p_a, the outflow is not actually choked, and the escape pressure is set to $p_e = p_a$ instead of the choke pressure.

Once the escape pressure and velocity (p_e and u_e) have been found, the other escape quantities, such as u_e, ρ_e and h_e, are found by using the equation of state at the point (p_e, s_0).

11

The final missing piece is then the decomposition of u_e into its components $u_{x,e}$ and $u_{y,e}$, i.e. finding the escape angle, θ_e. These may be found by considering entropy conservation of the total fluid model: since the flow equations without source terms conserve entropy, and the outflow model is isentropic by design, we may make the argument that the complete model in Eq. (4) should conserve entropy, to be consistent. Specifically, we demand that any entropy lost from the pipeline should be exactly equal to the entropy carried away by the loss of mass through the fracture. As it turns out, this leads to a unique constraint on the outflow angle, such that

$$u_{y,e} = \sqrt{u_e^2 - u^2}. \tag{12}$$

The above source-term calculation is repeated at every time step in the evolution of Eq. (4), in all cells along the pipeline, based on the current local averaged fluid state.

3.2.2. Numerical methods

The governing equations in (4) are discretized using the finite-volume method, and solved numerically employing a first-order single-stage two-cell MUSTA [59, 60] scheme. The time-step is limited by a Courant–Friedrichs–Lewy (CFL) condition for compressible flow, with a CFL number of 0.9.

3.3. The fluid-structure coupling

Even though two-curve methods consider the RDF as an uncoupled (fluid-structure) problem, an RDF in a pipeline truly represents a fluid-structure interaction (FSI) phenomenon. That is, it represents a problem where the boundary conditions for the fluid flow depend on the structure, and the response of the structure and crack-driving force are determined by the fluid behaviour.

In the pipeline-RDF model presented here, the equations governing the fluid flow and the response of the structure are treated as two computational fields and solved separately, with two distinct discretizations and numerical algorithms. The interfacial conditions (i.e., coupling between the solved equations) are used explicitly to communicate information between the fluid and structure solutions. This is also called a *partitioned approach* to an FSI problem [61].

A non-conforming mesh method, i.e., one that treats the fluid-structure boundary location and the related interface conditions as constraints imposed on the model equations, is used, such that non-conforming meshes can be employed. As a result, the fluid and solid equations can be conveniently solved independently from each other with their respective grids, and re-meshing is not necessary.

In addition to the forces exerted on the pipe by the internal fluid, external forces from geo-materials (and water in case of a subsea pipeline) will act on the pipe and absorb kinetic energy from the rapidly opening pipe. A third interaction will also take place between the escaping fluid and the backfill, but this will not be considered here. The current backfill model will be presented in Section 4.

3.3.1. The fluid-structure coupling scheme

In the coupled model, the following scheme, illustrated in Figure 5, is performed at each time step:

1. The structure model communicates the current fracture-width profile of each pipe cross-section along the pipe length $w_e(x)$ to the fluid model,
2. The fluid model uses this profile to integrate the fluid state to the current time,
3. The pressure profile for each cross-section along the pipe length for the current time is communicated back to the structure model,
4. The structure model uses the pressure profile at the current time to apply a load to its elements, and integrates the equations of the pipe material to the next time step.

In the cases run here, the time-step length required by the structure model is smaller than the one required by the fluid model. This means that stage 2 in the above scheme only involves a single time-step in the fluid model, smaller than what is required by the CFL criterion. Specifically for the present cases, the structure model requires a time-step of about 10^{-6} s, while the fluid model requires about 10^{-5} s.
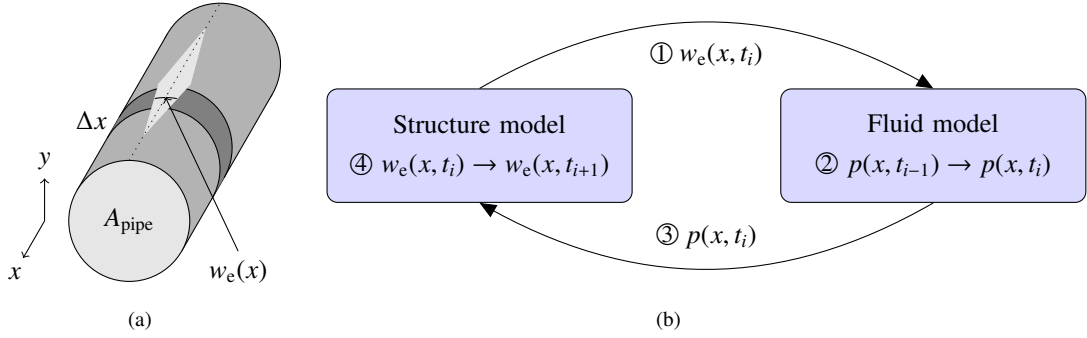
Figure 5: (a) Illustration of the pipeline as seen by the fluid. The fracture is represented by a fracture width $w_e(x)$, and the local fracture opening area is then $A_e = \Delta x \cdot w_e$. (b) Flow chart illustrating the coupling between the structure model and the fluid model.

3.3.2. Pressure-profile reconstruction at the opening fracture flaps

In several studies, the pressure on the opening fracture flaps was found to have a strong circumferential variation [24, 62, 63, 64]. Due to the huge cost in computational time associated with solving the full 3D fluid flow problem, a simplified or empirically-based pressure-profile reconstruction is normally used. From measurements in e.g. [24], a more than 50% difference in pressure from the top of the pipe (where pressure is at a minimum) to the bottom of the pipe (where pressure is maximum), was observed just 2–5 ms after the RDF had passed the axial location of the pressure sensors. Based on experimentally obtained pressure distributions from a 56 inch diameter pipe, an empirically based, exponential equation for the circumferential and longitudinal pressure variation was used in [25, 63, 64, 65].

Since the main crack-driving force for the RDF is the pressure from the CO_2 acting on the flaring pipe walls, it is important that the circumferential variation of the pressure be represented in a proper way. However, since we are here dealing with CO_2 in dense phase, phase change is involved during the outflow, and thus the common assumption of ideal gas cannot be used.

As shown in Section 3.2, the one-dimensional fluid model calculates two pressures at each axial computational cell: the cross-sectional average pressure p, and the escape pressure p_e. The latter represents the pressure at the fracture. For the fluid behaviour ahead of the propagating crack tip, where no circumferential variation in pressure is observed experimentally [24, 62, 64], the average pressure, p, is applied to all elements corresponding to each fluid computational cell in the structure model. Behind the crack tip, we model the circumferential pressure variation using the pressure-profile reconstruction described in the following. The reconstructed pressure provides an improved load estimate with respect to the cross-sectional average pressure.

At each axial position where the fracture has opened, the structure model communicates to the fluid model a set of cross-section profile widths at which pressure values are needed. For each axial position, the smallest of these widths is the fracture width $w_e(x)$, corresponding to the escape-area A_e in Eq. (7). The reconstructed pressure is then applied to all elements located between $w_e(x)$ and the largest of these widths, $w_M(x)$, while the elements below $w_M(x)$ are subjected to the average pressure (see Figure 6a).

To find the pressures to apply below the fracture opening, an additional estimate is performed for the vertical flow at each axial position. The outflow is calculated as quasi-steady isentropic compressible Bernoulli flow in a variable cross-section. Enforcing mass and energy conservation then leads to the equations

$$\rho(p, s_0)uw = C_1,$$
$$h(p, s_0) + \frac{1}{2}u^2 = C_2, \tag{13}$$

where w is the specified width, and C_1 and C_2 are constants. The above equations are then solved for p at each w using the known solution of p_e at w_e (fracture width) as a boundary condition.

However, during an RDF event, three main situations are met for the geometry of the pipe cross-section (Figure 6) and the following procedure is applied:

1. The cross-section has a circle-like shape with an opening without any flaps (Figure 6a): As described above,
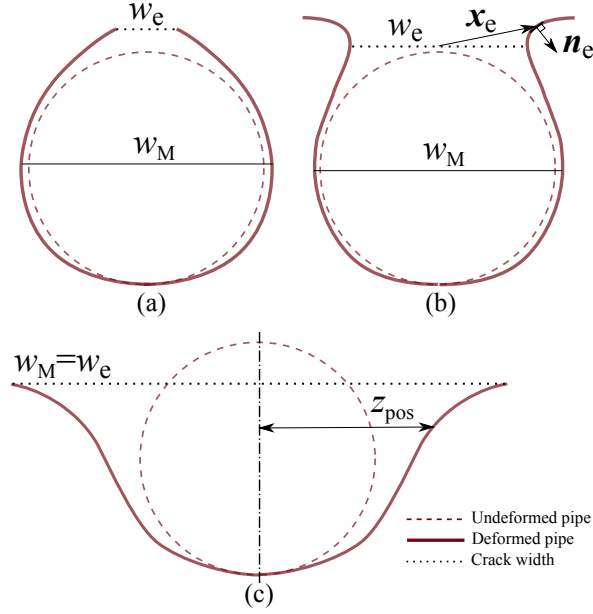
Figure 6: Illustration of the three different types of crack openings.

the pressure applied to the elements below the largest width, w_M, is the average pressure. The reconstructed pressure is applied to the elements between w_M and w_e.

2. The cross-section has a circle-like shape with flaps curving outwards beyond the opening (Figure 6b): The same methodology as for situation 1 is applied for elements at and below the opening at w_e. However, elements located on the flaps above w_e are subjected to a pressure equal to the escape pressure multiplied by the scalar-product of two unit vectors. The first vector, $\boldsymbol{x}_e$, is drawn from the middle of the w_e-line to the element's centre. The second vector, $\boldsymbol{n}_e$, is the element's outer normal vector. For elements where the scalar-product is negative, the pressure applied is 1 atm.

3. The cross-section has a V-like shape (Figure 6c): No reconstruction is performed, and the fluid code returns the escape pressure. In that case, all elements located within the diameter are subjected to the escape pressure while elements beyond are subjected to a pressure equal to the product of the escape pressure and the exponential decay $\exp\left(-z_{\text{pos}}/0.11D\right)$ where z_{pos} is the horizontal distance from the pipe axis and D is the current pipe diameter (after [25] and based on 3D fluid simulations).

4. The structure-backfill coupling and backfill representation

When pipelines are buried in soil [22, 66, 67] or surrounded by water [68, 69], the presence of this backfill slows down the speed of the RDF and decreases the required dynamic fracture toughness of the steel to arrest the fracture [68, 69]. In the following, we present a brief review on backfill effects on RDF followed by a description of the modelling approach for backfill used in this paper.

4.1. Review of backfill effects on the speed of an RDF

Backfill material on either side of the pipe acquires considerable kinetic energy from the flaring pipe walls following an RDF. In addition, the backfill material also dissipates energy from the expanding gas through plastic deformation (compression) and shear failure zones that are generated in the soil material [70], but this energy is rather small for many loose backfill materials compared to the kinetic energy uptake [22].
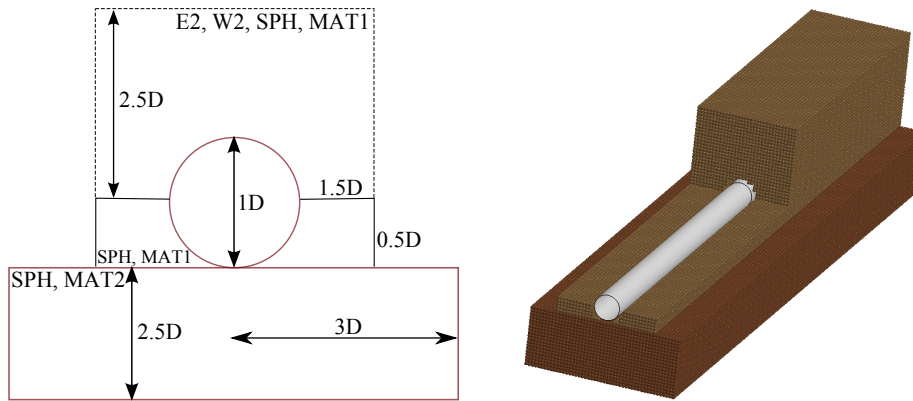
Figure 7: Left: Illustration of the geometry of the SPH backfill used in the model. Right: The FE model including the SPH particles.

The effect of backfill on the speed of an RDF is in the literature treated mainly empirically. In the equation for the fracture velocity used in the BTCM, the effect of backfill is described by a constant, and the fracture velocity is simply decreased by 28% or 39% when going from a pipe with no-backfill to a 0.76 m backfill or a water-submerged situation, respectively [67].

In [66, 67] the effects of backfill depth (inertial effects), soil stiffness, and soil strength were investigated. Relatively small effects of both the soil shear strength and the soil moisture content on the RDF speed were found. This is in agreement with the results of [69], where no significant effect on the RDF velocity when going from 3 inch to 10 feet backfill was seen. The RDF velocity seems relatively unaffected by soil density, but decreases slightly with an increase in soil shear strength and moisture content [66, 67]. The presence of the backfill will restrain the fracture opening as well as delay the escape of the leaking fluid. Both these effects effectively lead to an increase in the distance downstream from the crack-tip in which the pressure drops to 1 atm [22]. Among the coupled models found in the literature, only the works in [24] and [71] take explicitly into account (some of) the effects of backfill. In [24], backfill is modelled by increasing the pipe material density sufficiently to account for the soil inertia. In [71], soil is represented through lumped masses connected by spring elements. In [70], some interesting observations concerning a possible link between the mechanical response of the pipe support and crack arrest through ring-off are reported. It is hypothesized that ring-off in large-diameter pipelines can occur with a too loosely packed support allowing for a large bending moment in the pipeline which again leads to a biaxial stress state ahead of the crack tip where the axial stress is larger than the circumferential stress (see [72]).

It seems that only through a combination of experiments and fully coupled fluid-structure-backfill analyses can the effects of backfill, both on the fluid escape and on the restriction of movement of the fracture flaps, be studied and understood [22]. A model for backfill, taking into account both the effect of plastic dissipation and kinetic energy uptake of the soil will be presented in the following section.

4.2. The backfill model

Modelling of geo-materials such as sand, silt and clay, and in particular the simulation of large deformations and fracture of such inhomogeneous materials, is a challenging task. From a numerical point of view, soil can be either modelled as a granular material (particles) or as a continuum. In this paper, we choose to represent backfill using the smoothed particle hydrodynamics (SPH) method. SPH is a mesh-free Lagrangian method, that is well suited to describe granular materials under large deformations, see [73].

SPH is already implemented in LS-DYNA, and a wide range of constitutive material models exists, such as the Mohr-Coulomb model used here. An illustration of the current backfill geometry is shown in Figure 7. The contact between the SPH particles and the pipeline shell elements was modelled with a node-to-surface method, and a velocity independent coefficient of friction of 0.4. The default formulations and values from LS-DYNA for SPH and contact behaviour were used [39]. Two types of materials were used for the backfill representation, one for the compressed quarry plate where the pipes rest (MAT1), and one for the loosely compacted sand backfill (MAT2) on the sides of the test pipes (W1 and E1) and on top of the reservoir pipes (W2 and E2). A Mohr-Coulomb yield surface was used for

15

Table 5: Parameters used for the backfill materials. MAT1 corresponds to soft subbus (loosely packed sand on top) and MAT2 corresponds to clay. G is the elastic shear modulus, ν Poisson's ratio and ψ is the dilatation angle.

	Density (kg m^{-3})	G (MPa)	ν	ϕ (rad)	C (kPa)	ψ (rad)
MAT1	1700	8.0	0.2	0.61	0	0.61
MAT2	2000	18.5	0.35	0.61	0.5	0.61

the backfill materials. That is, the yield surface is given by

$$\tau_{max} = C + \sigma_n \cdot \tan\phi, \tag{14}$$

where τ_{max} is the maximum shear stress on any plane, σ_n is the normal stress on that plane and is positive in compression, C is the cohesion and ϕ is the friction angle. The tensile strength σ_{max} is given by

$$\sigma_{max} = \frac{C}{\tan\phi}, \tag{15}$$

where a reversible volumetric voiding takes place if the tensile stress exceeds σ_{max}. For a friction angle greater than zero, the Mohr-Coulomb yield surface implies a tensile pressure limit according to Eq. (15). The default behaviour is that voids develop in the material when this pressure limit is reached, and the pressure will never become more tensile than the pressure limit. Plastic strain is defined in the same way as in the elasto-plastic material model for the steels. The shear modulus, friction and dilatation angles, G, ϕ and ψ, respectively, are assumed not to vary with strain. Table 5 shows the parameters used for the two backfill materials.

5. Results

Results from the two crack-arrest tests described in Section 2 have been compared with results obtained from the coupled fluid-structure model described in Sections 3 and 4. The test results in each direction of crack growth, i.e. West and East, were considered separately for Test 1 and Test 2.

5.1. Simulation set-up

Measurements taken from the pressure transducers, timing wires and the observed final crack length in the two tests, were compared with the simulation results using the coupled model. A combination of shell elements and SPH particles was used to represent the steel and backfill material, respectively, employing about 60000 shell elements and about 300000 SPH particles. Symmetry boundary conditions were enforced on one side of the model, representing the boundary between East and West. Thus, it was assumed that there were no interactions between the two directions and that the crack propagated identically in both directions. The reservoir pipes (W2 and E2) were also included in the model but were given the same material properties as the test pipes, but with different thickness (according to values in Table 1). The material parameters defining the steel in the test pipes are shown in Table 4. No thermoplastic effects were considered, unless otherwise stated. Parameters for the backfill model are given in Table 5. The grid size for the fluid model was identical to the size of the elements along the pipe axis, i.e. about 15 mm.

5.2. Results overview

Figures 8 and 9 show the simulated and experimental results for Test 1 and Test 2, respectively, for both East and West direction, as defined in Section 2. In general, good agreement between the simulated and experimentally obtained data is seen. The jumps in fracture velocity in the experimental data are likely caused by scatter in the timing-wire data (see Section 2). Further, although the experimental fracture velocity measurements stop at around 3.5 m in Figure 8, the fractures in Test 1 did run the full length of the test section (see also Table 3).
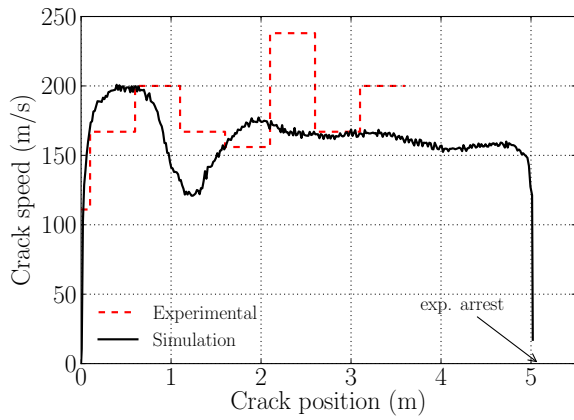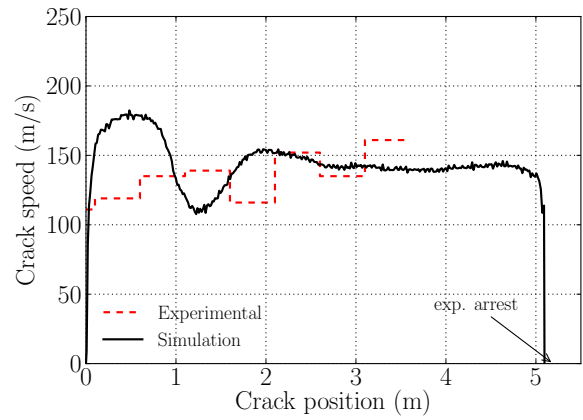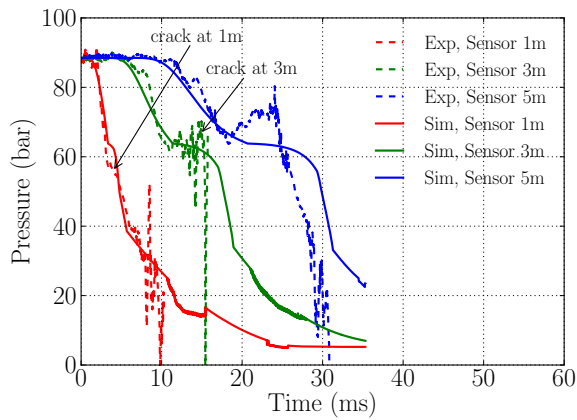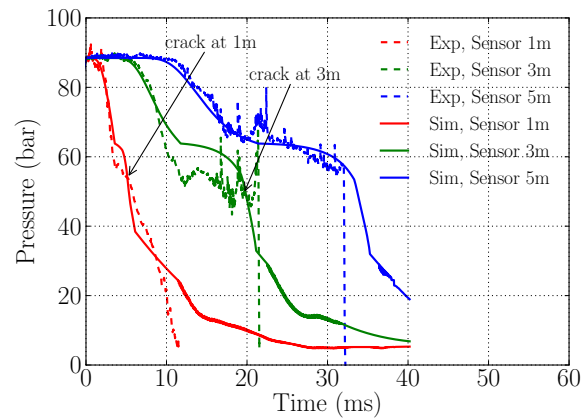
Figure 8: Results for Test 1 using the coupled model. Plots (a) and (b) show a comparison of the measured and simulated crack speed (v_f) as a function of crack position in the West and East direction, respectively. Note that experimental crack speeds are deduced from high-speed video and crack arrival time at the pressure sensors. Plots (c) and (d) show simulated (Sim) and measured (Exp) pressures at 1, 3 and 5 m from the girth weld joining the E1 and W1 pipes, in the West and East direction, respectively. The arrows in plots (c) and (d) indicate the crack arrival time at the 1 m and 3 m sensors.
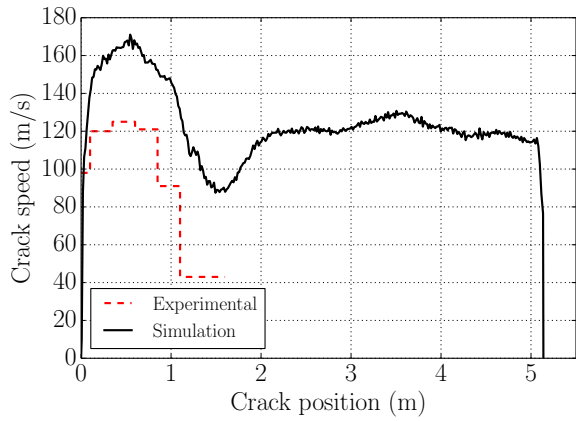
(a)
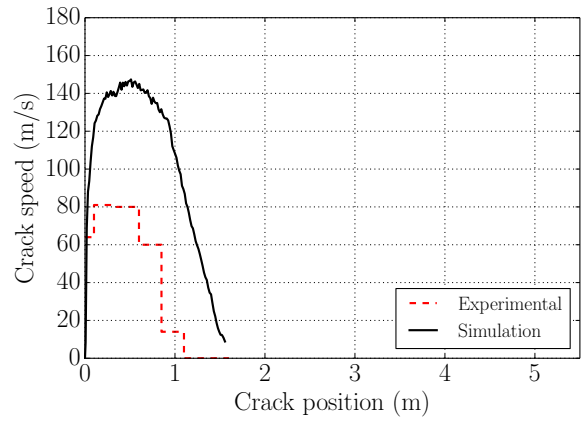
(b)
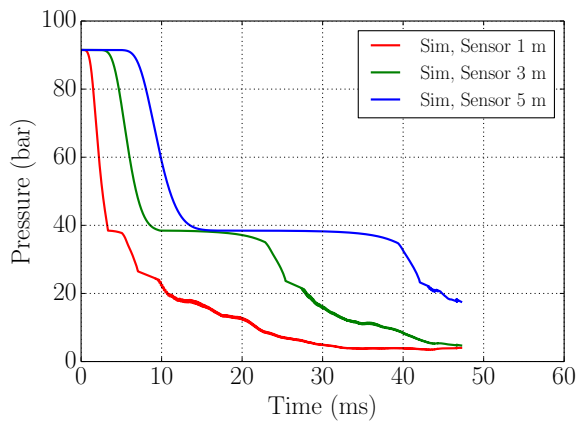
(c)
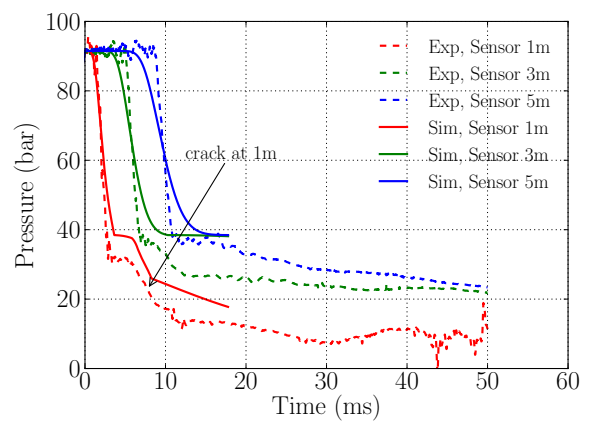
(d)

Figure 9: Results for Test 2 using the coupled model. Plots (a) and (b) show a comparison of measured and simulated crack speed (v_f) as a function of crack position in the West and East direction, respectively. Note that there were no experimental pressure data for Test 2 in West direction. Plots (c) and (d) show simulated (Sim) and measured (Exp) pressures at 1, 3 and 5 m from the girth weld joining the W1 and E1 pipes, in the West and East direction, respectively. The arrow in plot (d) indicates the crack arrival time at the 1 m sensor.

18
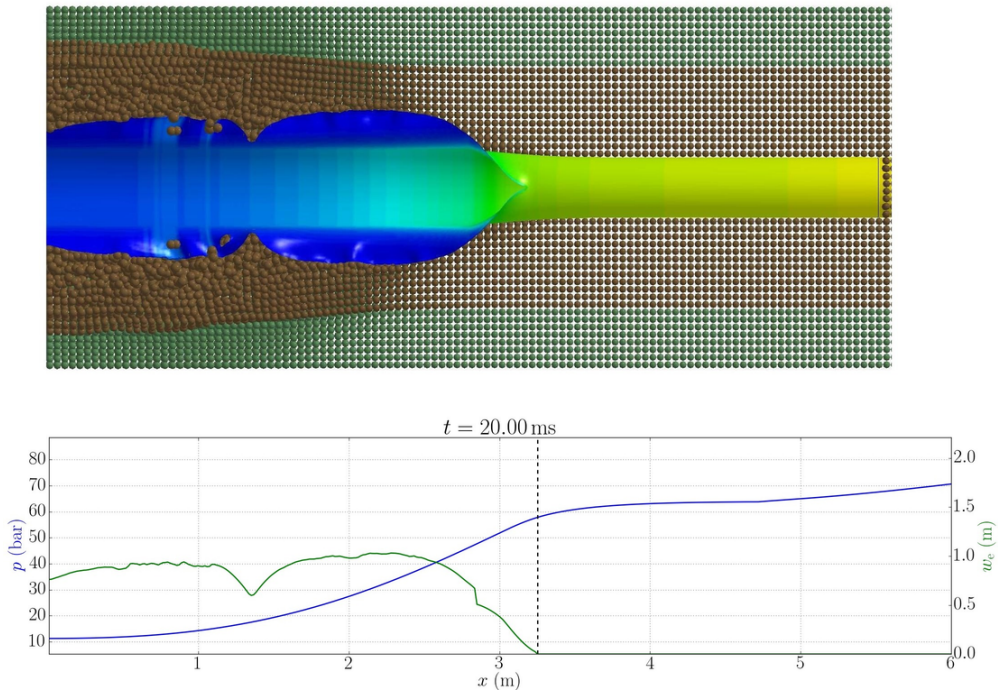
Figure 10: Visualization from coupled simulation of Test 1, pipe E1, 20 ms after the fracture initiation. The top picture shows the current structure coloured according to applied pressure, surrounded by SPH particles. The bottom graph shows the current average/1D pipeline pressure, and the current fracture width profile as seen by the fluid model (see also Figure 5).

5.3. Comparison of simulations with Test 1

For Test 1, excellent agreement between the simulated and experimental crack speeds as a function of crack position (relative to the end of initiation crack) can be seen in Figures 8a and 8b, for both West and East direction, respectively. A snapshot from the E1 simulation, showing structure, SPH particles and pipeline pressures, can be seen in Figure 10. Crack arrest through a ring-off at the welds between E1/E2 and between W1/W2 was observed both in the model and in the experiments. Although the simulations show a crack propagation along the girth welds to the reservoir pipes, the fluid-structure coupling scheme has not yet been specifically developed for the change of the crack direction in such situations. Note that beyond 3.5 m of crack propagation, no timing wires were placed, so no crack speed data exist between about 3.5 and 5 m.

In the first metre of crack propagation in the East direction (Figure 8b), the crack speed is overestimated by about $50 \, \mathrm{m\,s^{-1}}$. A possible explanation to this can be seen by studying the comparison of the simulated and experimentally measured crack-driving forces caused by the pressure. In general, an excellent agreement between the simulated and experimentally measured pressures (taken at 3 o'clock position in the pipe) can be seen in Figures 8c and 8d, for the West and East directions, respectively. However, the saturation pressure calculated by the fluid model (64 bar) for the initial conditions in Test 1 (see Table 3), is about 6–7 bar higher than the measured plateau pressure at the 1 m pressure sensor in both directions. While the 3 m sensor in the West direction shows excellent agreement with the model, the East direction 3 m sensor is still 6–7 bar lower than the model prediction. The experimental 5 m sensor data in the West direction show a sudden increase in pressure after the plateau has been reached. This remains unexplained, but could be due large vertical and horizontal velocities of the pipe sections at this point in the experiment. In general, a steadily improving agreement between the simulated and experimentally obtained pressure plateau can be observed as the pressure sensors are located further away from the initial crack. This trend is more clearly seen in Test 2. In our simulations, it is found that the pressure at the crack trip decreases as the crack propagates – down to the saturation pressure (64 bar) after 0.3 m propagation, and further to 56.8 bar after 4 m of crack propagation. This will be further illustrated in Section 6.

5.4. Comparison of simulations with Test 2

Regarding Test 2, despite that an early crack arrest is predicted by the BTCM methods (see Appendix A), and that this also was observed in the experiments, the coupled model predicts crack arrest only in the East direction (the thickest test pipe), as seen in Figures 9a and 9b. For the West direction, the simulation did not capture crack arrest as observed in the experiment. Possible reasons for this are discussed in Section 6. The predicted arrest length in the East direction (Figure 9b) is slightly longer than the observed arrest length. Similarly to Test 1 in East direction, in the first metre of crack propagation, the fracture velocity is overestimated by the model by about 50–70 m s^{-1}, and the calculated plateau pressure is overestimated by about 6–7 bar for the 1 m sensor in the East direction (Figure 9d). The experimentally measured pressure plateau increases up to the model-predicted value at the 3 m sensor position. No pressure sensors were used in the West direction experiment (Figure 9c). From Figure 9d it can also be observed that the pressure drop down to the plateau is more smeared out in the simulations than in the experiments. It should also be noted that the experiments show crack arrest through a ring-off in both test sections (see Figure 2). Except when the fracture propagates into a thicker material (as in Test 1), the model does not account for circumferential deviation of the straight fracture path.

As for Test 1, the simulated pressure at the crack tip decreases as the crack propagates – down to the saturation pressure (38.6 bar) after 0.2 m of propagation, and further down to 35.9 bar after 4 m of crack propagation. This is similar to the case of the two full-scale tests discussed by Cosham *et al.* [12], where a crack-tip pressure of 4–8 bar lower than the saturation pressure was measured. This will be further illustrated in Section 6.

6. Discussion

Based on the present results, one might be tempted to conclude that the two-curve methods (TCMs) are suited to determine the arrest versus no-arrest boundary for the steels and CO_2 initial conditions investigated here. As shown in Appendix A, the TCMs correctly predicted crack arrest in both test pipes in Test 2, and no arrest in either test pipe in Test 1. For dense-phase CO_2 pipelines, the estimated required CVP required for arrest (according to BTCM) as a function of the saturation pressure can be plotted, as done in [12], where the respective lines should separate the 'propagate' from the 'arrest' points. This plot is shown in Figure 11 for the two tests reported here. Note that no correction factor for CVP > 100 J has been performed for this plot, since this will not affect the conclusions from the two tests reported here. According to BTCM and Figure 11, there is in Test 1 no CVP value for the test pipes (E1 and W1) high enough to arrest an RDF (see also e.g. Figure A.15a). The reservoir pipes in Test 1 (W2 and E2) are shown to have sufficient properties for arrest. However, these arrests – that took place through a ring-off at the girth welds – were a result of a combination of higher wall thickness and a higher CVP, are here not considered as valid arrest points.

Due to the higher thickness for the reservoir pipes, the predicted required toughness for arrest (W2: 50 J, E2: 30 J), is much lower than the actual toughness (W2: ≈235 J, E2: ≈350 J). We see this in Figure 11, as the two arrest points of Test 1 are well within the arrest region. In Test 2, there are two arrest points, representing the arrest in E1 and W1, but these are – according to BTCM – about 100 J higher than what is needed to arrest the crack.

It is also common to present results from crack-arrest tests in a plot showing the predicted CVP (according to BTCM) required for arrest versus the actual CVP of the pipeline. In these plots, the 1:1 line separates 'arrest points' (CVP from pipes where arrest took place) and the 'propagation points' (CVP from pipes where the crack propagated through). In Figure 12, the results from [12] have been plotted together with the results from Test 2 in the current paper. As noted earlier, Test 1 did not result in any points in this plot. In [12], it is suggested that the line separating the arrest and propagation points seems to depend on the saturation pressure. In Figure 12 it is readily observed that the line separating the 'propagate points' from the 'arrest points' changes when the saturation pressure is changed. As mentioned earlier, when reducing the saturation pressure by 8 bar in [12], the predicted required Charpy energy for arrest must be multiplied by a factor of approximately 2 (the 1:2 line in Figure 12). Since there is no propagation point from the two experiments reported in this paper (the predicted arrest-CVP is undefined/infinite in Test 1), we can only speculate whether the arrest-propagation line is further reduced (the 1:4 line shown as an example) for the even lower resulting saturation pressure in Test 2. That is, it is rather uncertain at what CVP the fracture would have propagated through both the test pipes in Test 2. According to the 1:1 and 1:2 boundary lines in Figure 12, approximately 33 J or 66 J, respectively, would be sufficient for arrest. If we take the 1:4 line as the arrest-propagate boundary, the arrest

points obtained in Test 2 could potentially be on the borderline of no-arrest. This is supported by the simulation results of Test 2, in particular for the thinnest pipe in the West direction (W1, Figure 9c), where the coupled-model simulation did not predict crack arrest.

The plateau pressure arising from the discontinuity of the decompression speed is a key quantity. In the equilibrium model, this plateau pressure is equal to the thermodynamically predicted saturation pressure, which is why it is usually referred to as p_{sat}. However, as mentioned, the experimentally observed plateau pressure has been found to be lower than the saturation pressure, which may be due to non-equilibrium effects. To estimate the effect of this, a simulation of Test 2 West was performed where the saturation pressure was lowered to approximately the initially observed plateau pressure in Figure 9d. This was achieved by lowering the initial temperature, T_0, by 6 °C, leading to a saturation pressure of 33 bar in Test 2.

Experimental pressure data from Test 2 (see Figure 9d) indicate a plateau pressure of approximately 32 bar at the 1 m sensor and 37 bar at the 3 m sensor. As seen in Figure 13, lowering the saturation pressure by about 5–6 bar (Figure 13b) results in a rapid crack arrest (Figure 13a) as well as a final crack length close to the one measured in the experiment (1.4 m). These results both indicate that non-equilibrium effects may be important, and that the arrest seen in Test 2 West is much closer to the arrest/no-arrest borderline than the BTCM predicts.

To recapitulate, for the current Test 2, the BTCM predicted good clearance to the propagation boundary, while our simulation results indicated that the case might have been close to the boundary. For several of the cases discussed in [12], the BTCM predicted 'arrest' for experiments that did propagate. In the following, we will use insights from our coupled-model simulations to highlight what we think is one important reason for the lack of predictive capability of the BTCM for dense-phase CO_2 pipelines.

The fracture-velocity model in the BTCM (see Appendix A) is derived mainly by fitting measured fracture velocities from a great number of crack-arrest experiments involving mostly ideal gases (lean natural gas and air), but also with rich natural-gas compositions. Rich natural gases also have a plateau pressure for which the decompression speed is discontinuous, but the discontinuity is much smaller than for CO_2, see e.g. [11] or Figure 4 in [5]. This means that the crack-driving forces, namely the pressure distribution on the opening fracture flaps, is radically different when comparing RDF in pipelines containing rich and lean natural gases with those containing dense-phase CO_2. From experimental data and models (mostly for ideal gases) it is well known that the pressure-decay length – the length downstream of the fracture tip for which the pressure drops to a small level – is in the range 1–2 pipe diameters (e.g. [22, 62, 65]). As already seen in Figure 10, and in more detail in Figure 14, the pressure level on the opening fracture flaps is sustained at a high level for a significantly longer distance than what is typical for an ideal gas. In Figure 14, the pressure distribution on the fracture flaps is compared for three situations with similar fracture-opening profiles, fracture velocities, total fracture length (i.e., same position of fracture tip) and identical pipes, but with three different initial gas conditions. The ideal gas situation in Figure 14c shows that the pressure drops to almost atmospheric pressure around 2 pipe diameters behind the crack tip. For Test 1 and Test 2 in Figures 14a and 14b, respectively, the pressure is sustained at a very high level on the whole fracture-opening region. In Figure 10, where the fracture has propagated a much longer distance than in Figure 14, it is seen that the pressure level has dropped to about 20% of the fracture-tip pressure level at 5–6 pipe diameters behind the crack tip. Though this decay length will depend on e.g. the fracture velocity and the initial state of the CO_2, it will not drastically be decreased until the fracture velocity drops below the lowest value in the decompression-speed discontinuity (below 57 m s^{-1} in Test 1 and 28 m s^{-1} in Test 2).

As mentioned, the BTCM contain empirical expressions for the fracture velocity and the pressure at the tip of the fracture for which an RDF will arrest, see Eqs. (A.2)–(A.3) in Appendix A. They are based mostly on data for ideal gases. Therefore, the use of the proposed coupled model to deduce expressions which could be applicable to dense-phase CO_2 constitutes an interesting avenue for future work. Future work with the coupled model could also consider the recently proposed fracture-velocity model in [74], as well as suggested empirical models trying to include the effect of backfill depth [66, 74]. It is also interesting to note that in [74], a fracture-velocity model that is independent of the Charpy test is proposed.

7. Conclusion

A coupled fluid-structure model for the prediction of running-ductile fracture (RDF) in CO_2-transport pipelines has been presented. The fluid flow inside the pipe, and out of the pipe through the fracture, is computed using a
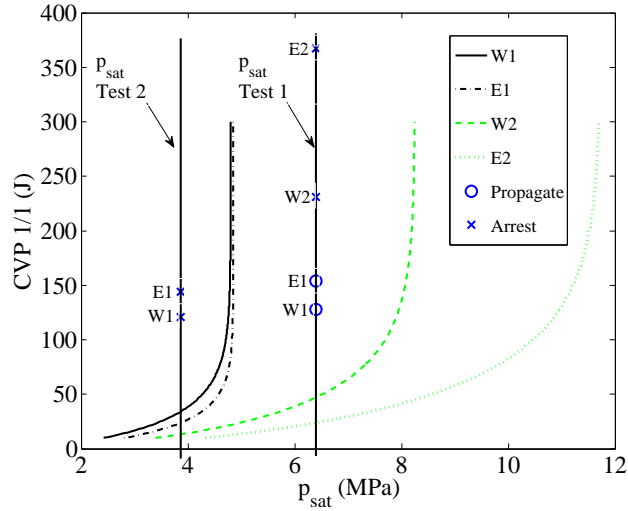
Figure 11: The required CVP energy for arrest as a function of the saturation pressure (p_{sat}) according to Eq. (A.3) ($p_{sat} = p_a$). Actual tests may be plotted according to their fluid saturation pressure and pipeline CVP. According to the arrest criterion $p_{sat} < p_a$, tests above and to the left of their corresponding curve are expected to arrest. Here, the experiments are marked as points, and labelled according to observed propagation or arrest.
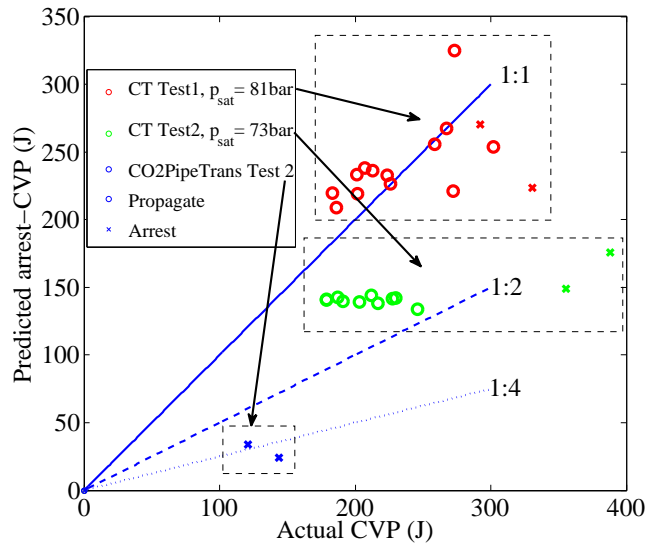
Figure 12: The predicted (Wilkowski *et al.* [75] correction factor used) arrest-toughness versus the actual toughness values from both the two full-scale COOLTRANS (CT) experiments [12] and from Test 2 reported here. The lines indicate the 1:1, 1:2 and 1:4 lines separating the arrest and propagate points for the different saturation pressures.

22
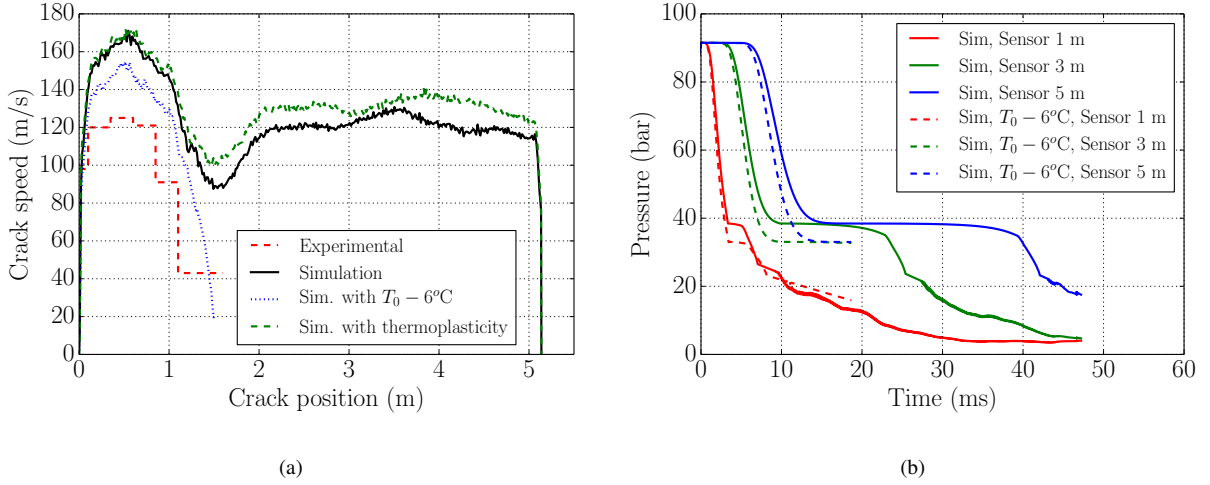
Figure 13: The effect of lowering T_0 by $6\,°C$ in Test 2 West direction on (a) the crack speed and (b) on the pressure readings. In (a) the effect of including thermoplastic effects in the constitutive equation (1) is also seen ($T_i = 281.6\,K$, $T_r = 300\,K$, $T_m = 1800\,K$, $m = 1.0$).

one-dimensional homogeneous equilibrium model (HEM). The thermodynamic properties of pure CO_2 are calculated with the Span–Wagner reference equation of state. The formation of solid CO_2 for pressures at and below the triple point is accounted for. The pipe material and the fracture are represented by a finite-element model employing shell elements and an elastic-plastic constitutive equation with a local ductile fracture criterion. The backfill, i.e. the soil material surrounding the pipe, is taken into consideration by a smoothed particle hydrodynamics (SPH) model.

The most common engineering tools in use today for fracture-propagation control, the two-curve methods, have been deemed by some researchers not to be applicable to pipelines carrying dense-phase CO_2 or CO_2-rich mixtures. Our working hypothesis is that by adding more physics, a better predictive capability may be attained, albeit at the cost of increased model complexity. This includes predictions over larger parameter ranges and a reduced need for full- and medium-scale testing to fit parameters.

Coupled-model predictions have been compared with experimental data for two medium-scale crack-arrest experiments for pure CO_2. Good agreement was observed, for pressures, fracture velocities as well as fracture lengths. In one of the cases (Test 2 West), fracture arrest was observed experimentally, but not in the simulations. Comparison between experimental data and model calculations showed that the calculated 'plateau pressure' was too high. There may be several causes for this. One hypothesis is that the assumption of thermodynamic equilibrium should be relaxed. This constitutes future work. However, an indication of the effect was obtained by lowering the initial temperature in the model calculations by $6\,°C$, which led to arrest in the coupled model as well. This also suggests that this case was sensitive to the initial conditions. Furthermore, our results corroborate one of the observations in [11], that the CVP impact energy may not be a sufficient measure to find the border between arrest and no-arrest for CO_2 pipelines.

Simulations have been performed to compare RDF in CO_2 and natural-gas pipelines. The results showed that for CO_2, the pressure at the opening fracture flaps was sustained at a high level at a significantly longer distance behind the crack tip. We suggest that this is one important reason why existing two-curve methods do not work for CO_2 pipelines.

In the future, we aim to investigate the effect of non-equilibrium, to extend the model to account for CO_2-rich mixtures, and to account for ring-off, in which the fracture deviates from a straight path.

Acknowledgements

23
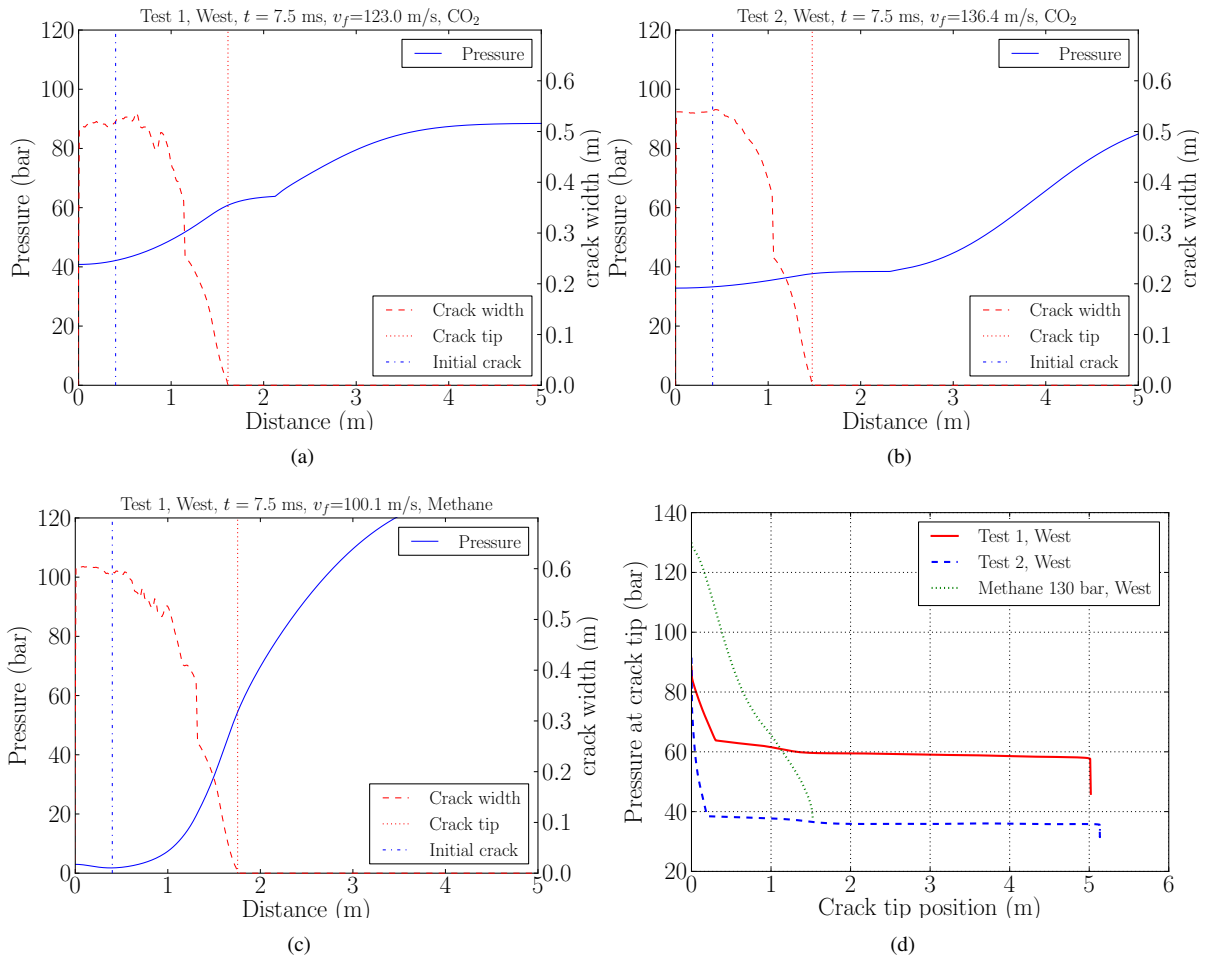
Figure 14: The average cross-section pressure as a function of position in the pipe for three simulated cases with the same material properties and pipeline dimensions and different fluid properties, but at the same time in the simulation where the crack opening profile, crack speed and crack tip pressure are of comparable magnitude. (a) Test 1, West pipe (b) Test 2, West pipe (c) Methane at initial pressure 130 bar and (d) Pressure at crack tip for cases (a), (b), (c).

Appendix A. Uncoupled two-curve models

Recent full-scale crack-arrest experiments [12] have shown that the current engineering methods are not applicable to address FPC and ensure rapid crack arrest in dense-phase CO_2 pipelines. In the following we will briefly review these methods, also known as the two-curve methods (TCMs). This is done to illustrate both the industrial need for the type of model presented in this paper and possible reasons why the TCMs are not applicable to dense-phase CO_2-transporting pipelines.

The TCMs, initially developed at the Battelle Memorial Institute in the 1970s [20], and further developed throughout the years, rely on the fundamental assumption that the decompression wave speed may be uncoupled from the fracture speed. This means that the decompression wave speed, Eq. (A.7), is calculated for an ideal full-bore opening decompression event, without the presence of a running fracture. The fracture speed, Eq. (A.3), is calculated as a simple (mainly empirical) function of the pressure at the crack tip, the pipe geometry and properties of the pipe material. No other interaction between the pipe material and the fluid is taken into account. The above considerations are often turned into curves for the decompression speed vs. pressure and fracture speed vs. pressure (hence *two-curve methods*, see Figure A.15), where it is said that a running fracture cannot be sustained if the fracture speed is lower than the decompression speed for all relevant pressures at the crack tip.

During decompression of dense-phase CO_2 for usual operating conditions, at some point the fluid state will go from single-phase liquid to two-phase. At this point, the decompression speed drops from somewhere around 300–$600\,\mathrm{m\,s^{-1}}$ to a value which is often below $100\,\mathrm{m\,s^{-1}}$. For an equilibrium state, this happens at the saturation pressure, and it is often referred to as the 'plateau pressure'. The TCMs were developed for gas mixtures where the decompression speed decreases continuously with the pressure, with possible extensions to rich natural gases where a two-phase behaviour can cause a small discontinuous drop at rather high decompression speeds. The decompression-speed discontinuity for CO_2 is usually much larger.

In general, and dependent on the initial CO_2 conditions, the fracture speed at the saturation pressure is usually within the discontinuity of the decompression speed. In other words, the pressure levels just above (liquid state) move faster than the fracture, and the pressure levels just below (liquid–vapour state) move slower than the fracture. In steady conditions, the crack tip of a propagating ductile fracture will therefore most likely stay at the plateau, and see a pressure close to the saturation pressure of the CO_2.

In the TCMs, it is assumed that conditions for initiation of ductile crack growth and arrest of an RDF are the same (e.g. [20, 76]). These methods provide an expression for the 'arrest pressure', which is the pressure at the crack tip for which neither crack growth initiation, nor further crack propagation, can take place. According to the TCMs, conditions for crack arrest in a pipeline transporting dense-phase CO_2 can therefore be reduced to the question whether the saturation pressure is lower or higher than the arrest pressure [11]. However, the only reported full-scale fracture-arrest experiment for dense-phase CO_2 [12] shows that a TCM grossly underpredicts the needed material properties for crack arrest.

In the following, we present the two curves of the TCMs, employing a unified formulation.

Appendix A.1. Fracture-speed models

In the Battelle TCM [20] the axial propagation speed of the fracture, v_f, is covered by the theory of plastic wave propagation in solids. The speed of a propagating plastic wave, v, can be written as

$$v = \sqrt{\frac{P}{\rho}}, \tag{A.1}$$

where ρ is the material density and P is the tangent modulus of the engineering stress-strain curve at a particular strain that characterizes the wave. A derivation of v_f from Eq. (A.1) – shown in full detail in [74] – shows that v_f can be

Table A.6: Quantities in Eq. (A.2) and Eq. (A.3) which depend on the model used.

	Battelle	HLP (original)	HLP (Sumitomo)
α	C	α_0	$\alpha_0 \left(\frac{Dt}{D_0 t_0}\right)^{\frac{1}{4}}$
β	$1/6$	β_0	$\beta_0 \left(\frac{D}{D_0}\right)^{\frac{5}{2}} \left(\frac{t}{t_0}\right)^{-\frac{1}{2}}$
γ	1	1	$3.42 \cdot \left[3.22 + 0.20\left(\frac{t/D}{t_0/D_0}\right)^3\right]^{-1}$
R_f	$E_{\text{CVP}}/A_{\text{CVP}}$	$E_{\text{DWTT}}/A_{\text{DWTT}}$	$E_{\text{DWTT}}/A_{\text{DWTT}}$

written as

$$v_{\text{f}}(p) = \begin{cases} \alpha \frac{\bar{\sigma}}{\sqrt{R_{\text{f}}}} \left(\frac{p}{p_{\text{a}}} - 1\right)^{\beta} & \text{if } p > p_{\text{a}}, \\ 0 & \text{if } p \leq p_{\text{a}}, \end{cases} \tag{A.2}$$

where the arrest pressure, p_{a}, is defined as

$$p_a = \gamma \cdot \frac{2t\bar{\sigma}}{3.33\pi R} \arccos\left[\exp\left(-\frac{\pi R_{\text{f}} E}{24\bar{\sigma}^2 \sqrt{Rt}}\right)\right]. \tag{A.3}$$

Here $\bar{\sigma}$ (Pa) is the material flow stress, R_{f} (J/m^2) is the Charpy plateau energy per fracture area, t (m) is the pipeline wall thickness, R (m) is the outer pipeline radius and E (Pa) is the material elastic modulus.

This original model was further elaborated by the High Strength Line Pipe (HLP) Committee [77, 78], and again extended with more parameters in the form of *the Sumitomo version* [21]. These models appear in a variety of forms in the literature, due to differing systems of units and various merging of variables and constants. Though it might not appear so at first sight, all the previously mentioned uncoupled models may in fact be unified to the same form, where the quantities α (m^2/kg$^{0.5}$), β ($-$), γ ($-$) and R_{f} (J/m^2) are quantities which depend on the specific model, as indicated in Table A.6 and discussed in Appendix B. The flow stress is defined differently for the various methods. For Battelle, $\bar{\sigma} = \sigma_0 + 68.95$ MPa, and for the HLP methods, $\bar{\sigma} = 0.5(\sigma_0 + \sigma_{\text{TS}})$. Note that for all uncoupled models, as the magnitude of the term in the exponential function in Eq. (A.3) grows large,

$$p_{\text{a}} \to \frac{\gamma t\bar{\sigma}}{3.33R}. \tag{A.4}$$

This means that the arrest pressure saturates as a function of material toughness, and becomes independent of it. This limit can be reached with real high-toughness steels. For the steels used in the test pipes (E1 and W1) investigated here, the arccos term in Eq. (A.3) is always within 0.5% of $\pi/2$.

As seen in Table A.6, there are two different measures of material toughness used: $E_{\text{CVP}}/A_{\text{CVP}}$ (J/m^2) is the full-size upper-shelf Charpy V-notch energy per fracture area, and $E_{\text{DWTT}}/A_{\text{DWTT}}$ (J/m^2) is the pre-cracked thickness drop weight tear test (DWTT) energy per area. In this work, only E_{CVP} was measured directly, and E_{DWTT} was calculated according to the correlation [78]

$$E_{\text{DWTT}}(\text{J}) = 3.29 \, \text{J}^{0.456}\text{mm}^{-1.5} \times t(\text{mm})^{1.5} \times E_{\text{CVP}}(\text{J})^{0.544}, \tag{A.5}$$

and divided by the area (according to ASTM E436) $A_{\text{DWTT}} = t \times (76\,\text{mm} - 5\,\text{mm})$ to yield a value for R_{f}. In the cases studied here, the estimated DWTT R_{f} values differ from the Charpy R_{f} values by no more than about 10%.

The constant β_0 is always equal to 0.393, while the quantities C and α_0 supposedly only depend on the amount of backfill (none, soil, water) above the pipeline. Even in the case of no backfill, it is implied that the pipeline is below ground level in a ditch. To our knowledge, no parameters have been fitted to experiments with pipelines on flat ground. Here, the experiments were performed with no backfill (in a ditch), in which case $C = 0.379 \times 10^{-3}$ m^{2}kg$^{-0.5}$ [67]. In addition, no reference to α_0 for no backfill can be found in the literature. From [20] it is found that C is 28% higher in conditions without backfill than when backfill (0.76 m) is present. We choose to apply the same scaling when going to conditions without backfill for α_0, and get $\alpha_0 = 0.925 \times 10^{-3}$ m^{2}kg$^{-0.5}$. The reference geometry for the fitting of α and β is $D_0 = 1219.2$ mm and $t_0 = 18.3$ mm, with $D = 2R$ being the outer pipeline diameter.

Appendix A.2. Decompression speed

The model for gas decompression speed in the two-curve methods is derived by considering a pipeline with a stationary fluid at a given initial pressure, and which is suddenly opened at one end. The opening is completely stationary, as opposed to being a running fracture. By assuming one-dimensional and isentropic flow, one may analyse the characteristics of the Euler equations to show that along a rarefaction wave, the fluid velocity relates to the pressure as

$$\frac{\mathrm{d}|u|}{\mathrm{d}p} = -\frac{1}{\rho c}, \tag{A.6}$$

where ρ is the local density and c is the local speed of sound. This is called the *real fluid isentropic decompression model*, and shows that the absolute value of the fluid velocity is larger the further down one is on the pressure curve, i.e. the closer one is to the opening. Since a pressure wave moves at the local speed of sound relative to the fluid, and the initial fluid velocity is zero, the speed of a pressure level relative to the pipeline is given by

$$
\begin{aligned}
v(p) &= c(p) - |u(p)| \\
&= c(p) - \int_p^{p_i} \frac{1}{\rho(p')c(p')} \mathrm{d}p'.
\end{aligned} \tag{A.7}
$$

With an equation of state to find the isentropic ρ and c, Eq. (A.7) may be used to draw the decompression-speed curve in two-curve methods. It should be noted that the above approach, when used for multiphase flow, assumes no slip between the phases.

Appendix A.3. Two-curve analysis

The fracture-speed curve for the pipeline, from Appendix A.1, and the decompression speed curve for the fluid, from Appendix A.2, may be used to perform two-curve analysis. This simply entails plotting the two curves together, and comparing the velocities across the pressure range below the initial pressure. If there exists a pressure where the fracture tip will be faster than the decompression wave, the fracture will run ahead, and there is no arrest. If not, the pressure wave will run ahead, the pressure will drop at the fracture tip, and there is arrest. We remark that here, the Wilkowski *et al.* [75] correction method for v_f at high CVP values has not been applied.

Appendix A.4. Fracture length

The uncoupled models may also be used to estimate the position of the fracture tip as a function of time. In the cases where the two-curve analysis predicts fracture arrest, this may then be used to estimate the final fracture length. When one has an equation for the fracture velocity given a fluid pressure at the fracture tip, $v_f(p)$, and an equation for finding the fluid pressure level at a given decompression speed, $p_{\text{decomp}}(v)$, one may derive an ordinary differential equation (ODE) for the fracture tip position, L. The function $v_f(p)$ is given by fracture-velocity models such as Eq. (A.2). The function $p_{\text{decomp}}(v)$ is found from the decompression model in Eq. (A.6), by interpolating an obtained $v(p)$ curve.

The derivative of L with respect to the time, t, is equal to the fracture velocity, $v_f(p)$, by definition. To evaluate the latter at a given time, one needs the fluid pressure at the fracture tip position at that time. Under the assumptions that the decompression process is unaffected by the presence of the running fracture, and that the decompression starts at the point $L = 0$ at time $t = 0$, this pressure is simply given by the fluid pressure level which moves at a velocity L/t in the decompression model. The ODE resulting from these assumptions is

$$\frac{\mathrm{d}L}{\mathrm{d}t} = v_f \tag{A.8}$$

$$= v_f(p_{\text{tip}}(L,t)) \tag{A.9}$$

$$= v_f(p_{\text{decomp}}(L/t)), \tag{A.10}$$

which may be integrated numerically until arrest is reached, giving a final arrest length, L_a. To obtain a solution, initial conditions are also needed. The approach used with the HLP model [21, 78], is to set L_0 equal to the pipeline diameter. One may also consider the experimental initial fracture length. In the case studied here, there is little distinction between the two, and the latter is used.

Table A.7: Results from two-curve analysis of the test sections W1 and E1, for Test 1 and Test 2. The numbers presented here are from using the worst-case initial condition ($t_0 = 0$), giving the fastest and longest fractures. The given fracture lengths are in addition to the 40 cm initial length.

	p_{sat} (bar)		Battelle			HLP (orig.)			HLP (Sum.)		
			p_a (bar)	L_a (cm)	t_a (ms)	p_a (bar)	L_a (cm)	t_a (ms)	p_a (bar)	L_a (cm)	t_a (ms)
Test 1	64.0	W1	46.9	∞	∞	46.4	∞	∞	46.2	∞	∞
		E1	47.8	∞	∞	47.0	∞	∞	44.1	∞	∞
Test 2	38.6	W1	46.7	18	1.2	46.2	100	2.8	46.2	31	1.4
		E1	46.2	11	1.0	46.0	40	1.6	43.3	19	1.2

There is also an issue of how much head-start the fracture should get in front of the decompression wave, which is specified through the initial time, t_0, of the above ODE integration. Since the most correct choice is not known, we use two assumptions on each side of the reasonable area. The first is $t_0 = 0.0$, which represents a maximal head-start for the fracture, i.e., a full-bore opening at the centre at the same time as the fracture starts at L_0. The second is $t_0 = L_0/v_i$, where v_i is the decompression speed of the initial pressure level. This corresponds to the front of the pressure drop being at the fracture tip when the fracture starts running, i.e. no head-start.

Appendix A.5. Uncoupled/two-curve analysis

The experimental cases were also analysed using the uncoupled models described above, employing parameters from Tables 1 and 2, and a standard elastic modulus of 200 GPa. The results of the two-curve analysis can be seen in Figure A.15. For the test sections W1 and E1, all versions of the model correctly predict no-arrest/RDF in Test 1, and arrest in Test 2.

Even though the TCMs were originally developed only to provide a yes/no criterion for crack arrest, we would like to illustrate the model properties in more detail. For Test 2, which showed arrest, fracture-length estimation was performed according to Appendix A.4, for both assumptions for fracture head-start. The assumption of $t_0 = L_0/v_i$ predicted extremely short fractures. The results from the most conservative assumption, $t_0 = 0$, i.e. the one giving the longest fractures, are given in Table A.7. It appears that all the uncoupled models underestimate the fracture length after arrest, with only HLP (orig.) being reasonably close, underpredicting by 30% (W1) and 60% (E1). All of them vastly underpredict the arrest time by more than one order of magnitude (see Table 3).

Also seen in Figure A.15 are the experimental average fracture speeds in W1 and E1. In the cases with RDF, one expects an average fracture speed somewhere between the speed at the initial pressure and the steady-state speed at the rightmost intersection with the decompression speed. If the initial fracture speed is larger than the initial decompression speed, one expects the fracture to retain the initial speed. Given this, we see in Figures A.15a, A.15c and A.15e that the Battelle model underpredicts the average fracture speed, and both HLP models overpredict it. In the cases with fracture arrest, one expects an average fracture speed somewhere between zero and the speed at the initial pressure. Given this, we see in Figures A.15b, A.15d and A.15f that all the models have the observed speed within this region.

Appendix B. Uncoupled models in SI units

When surveying the literature for the uncoupled models, it is easy to get confused due to the varying conventions. The fitted constants are not dimensionless, and thus one must be careful not to apply the numerical values fitted with one convention to equations in another convention. Additionally, in some conventions, constants are added in order to correct for the use of inconsistent units, and some may even include hidden unrelated quantities such as the fracture area used when testing the toughness of the pipeline material. This appendix aims to briefly document the transformation from conventions found in the literature, to the consistent SI-unit representation used in this work ((A.2) and (A.3)).

In the following equations, a variable without a unit label implicitly has the corresponding standard non-prefixed SI unit.
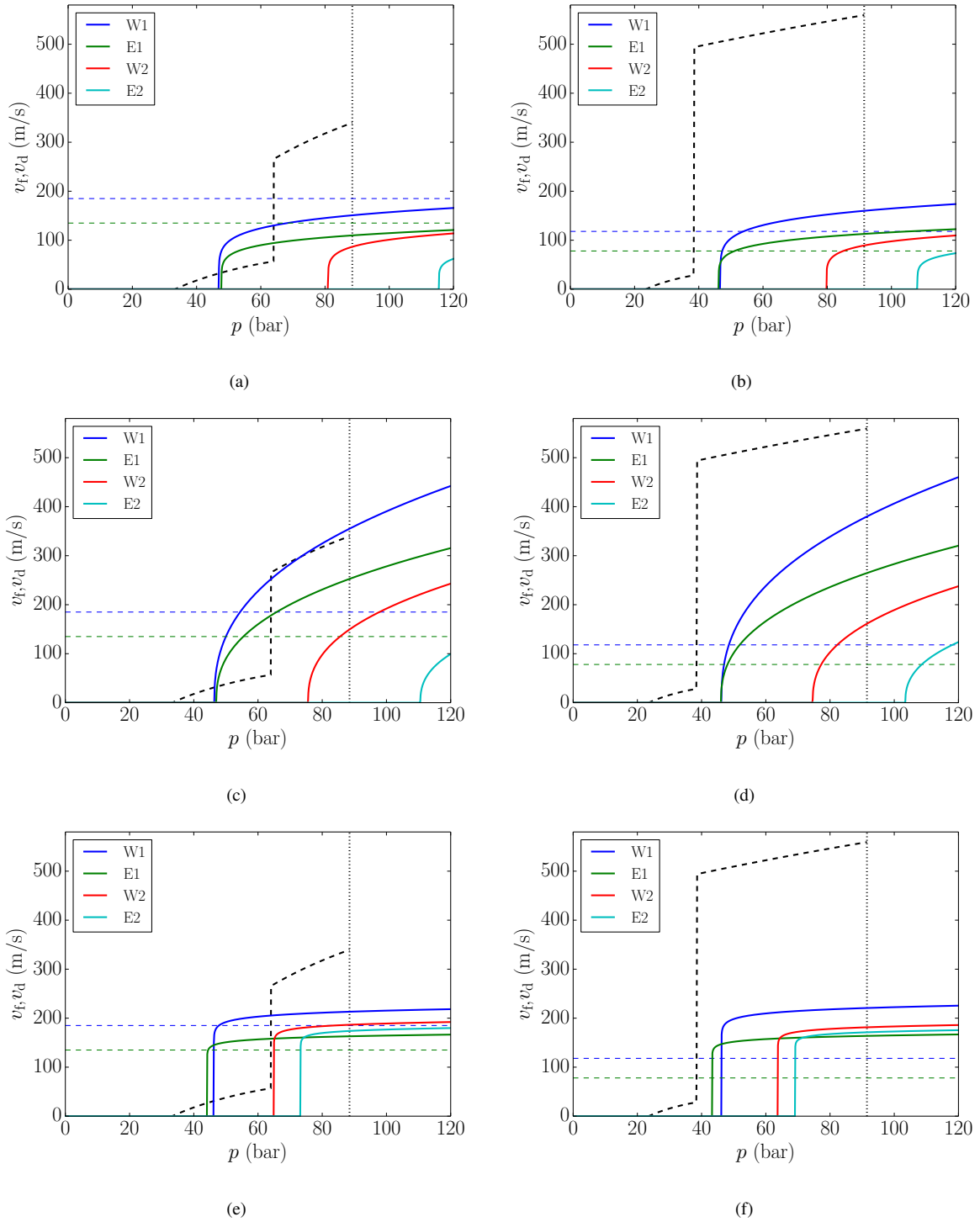
Figure A.15: Results from the Battelle and HLP two-curve analysis for (a) Test 1 with Battelle, (b) Test 2 with Battelle, (c) Test 1 with HLP(orig.), (d) Test 2 with HLP(orig.), (e) Test 1 with HLP(Sum.), and (f) Test 2 with HLP(Sum.) The solid curves show the fracture speeds for each of the four pipelines, and the dashed curve shows the decompression speeds for CO_2. The vertical dotted line marks the initial pressure, and the horizontal dashed lines mark the experimental average fracture speeds from Table 3, for W1 and E1.

Appendix B.1. Battelle

This section will outline how to transform the representation of the Battelle method found in [67] to the form used in this work. In the equations for the arrest stress and fracture velocity, it is the intrinsic material property of fracture energy per area ($E_{\mathrm{CVP}}/A_{\mathrm{CVP}}$) which is relevant, but in Eqs. (1) and (2) in [67] the quantity E_{CVP} appears alone. This is because this formulation has implicitly assumed that all Charpy toughness tests have been performed with a '2/3 size specimen', of area $2/3 \cdot 80\,\mathrm{mm}^2$. When untangling the specimen area from the constants, while transforming to a form with consistent SI units, the first parenthesis of Eq. (1) in [67] becomes

$$C'(\mathrm{m\,J^{0.5}\,s^{-1}\,MPa^{-1}})\frac{\bar{\sigma}(\mathrm{MPa})}{\sqrt{E_{\mathrm{CVP}}(\mathrm{J})}} = C'(\mathrm{m\,J^{0.5}\,s^{-1}\,MPa^{-1})}\frac{10^{-6}(\mathrm{MPa/Pa})}{\sqrt{\frac{2}{3}80\cdot10^{-6}}(\mathrm{m})}\frac{\bar{\sigma}}{\sqrt{E_{\mathrm{CVP}}/A_{\mathrm{CVP}}}}$$

$$= \left(C'\frac{10^{-3}}{\sqrt{\frac{2}{3}80}}\right)(\mathrm{m^2\,kg^{-0.5}})\frac{\bar{\sigma}}{\sqrt{E_{\mathrm{CVP}}/A_{\mathrm{CVP}}}}, \tag{B.1}$$

while the exponent of Eq. (2) in [67] becomes

$$\frac{\pi\cdot18.75(\mathrm{mm\,MPa\,J^{-1}})\cdot E_{\mathrm{CVP}}\cdot E(\mathrm{MPa})}{24\cdot\bar{\sigma}^2(\mathrm{MPa})\cdot\sqrt{R(\mathrm{mm})t(\mathrm{mm})}}$$

$$= \frac{18.75(\mathrm{mm\,MPa\,J^{-1}})\cdot\left(\frac{2}{3}80\cdot10^{-6}\right)(\mathrm{m^2})\cdot10^{-6}(\mathrm{MPa/Pa})}{10^{-12}(\mathrm{MPa^2/Pa^2})\cdot10^3(\mathrm{mm/m})}\frac{\pi(E_{\mathrm{CVP}}/A_{\mathrm{CVP}})E}{24\bar{\sigma}^2\sqrt{Rt}} = \frac{\pi(E_{\mathrm{CVP}}/A_{\mathrm{CVP}})E}{24\bar{\sigma}^2\sqrt{Rt}}. \tag{B.2}$$

Notice how the factor 18.75 in Eq. (B.2) is purely an effect of unit corrections and the 'hiding' of A, and disappears completely in the formulation used here. In some works, the factor appears to be 10 instead of 18.75, in which case the specimen area A is not included, and a different set of units is used.

Appendix B.2. HLP

When changing to consistent SI units, the first part of Eq. (6) in [21] transforms as

$$\alpha'(\mathrm{J^{0.5}\,m\,mm^{-1}\,s^{-1}\,MPa^{-1}})\frac{\bar{\sigma}(\mathrm{MPa})}{\sqrt{E_{\mathrm{DWTT}}/(A_{\mathrm{DWTT}}(\mathrm{mm}^2))}} = \left(\alpha'\cdot10^{-3}\right)(\mathrm{m^2\,kg^{-0.5}})\frac{\bar{\sigma}}{\sqrt{E_{\mathrm{DWTT}}/A_{\mathrm{DWTT}}}}, \tag{B.3}$$

while the exponent of Eq. (7) in [21] transforms as

$$\frac{E_{\mathrm{DWTT}}/(A_{\mathrm{DWTT}}(\mathrm{mm^2}))K'(\mathrm{MPa^2\,mm^3\,J^{-1}})}{\bar{\sigma}^2(\mathrm{MPa})\sqrt{D(\mathrm{mm})t(\mathrm{mm})}} = \frac{E_{\mathrm{DWTT}}/A_{\mathrm{DWTT}}\cdot10^{-6}(\mathrm{m^2/mm^2})\cdot K'(\mathrm{MPa^2\,mm^3\,J^{-1}})}{\bar{\sigma}^2\cdot10^{-12}(\mathrm{MPa^2/Pa^2})\cdot\sqrt{Dt}\cdot10^3(\mathrm{mm/m})}$$

$$= \left(K'\cdot10^3\right)(\mathrm{Pa})\cdot\frac{E_{\mathrm{DWTT}}/A_{\mathrm{DWTT}}}{\bar{\sigma}^2\cdot\sqrt{Dt}}. \tag{B.4}$$

To highlight the similarities between the two uncoupled methods, the prefactor of Eq. (7) in [21] may be transformed as

$$0.382\cdot\frac{t\bar{\sigma}}{D} = \frac{2t\bar{\sigma}}{3.33\pi R}. \tag{B.5}$$

Finally, we have used the fact that the constant in the exponent of Eq. (7) in [21] actually is a collection of constants including E:

$$K = K'\cdot10^3 = \frac{\sqrt{2}\pi E}{24}. \tag{B.6}$$

References

[1] T. F. Stocker, D. Qin, G.-K. Plattner, M. Tignor, S. Allen, J. Boschung, A. Nauels, Y. Xia, V. Bex, P. M. (eds.), Climate change 2013: The physical science basis, Tech. rep., Working Group I Contribution to the Fifth Assessment Report of the Intergovernmental Panel on Climate Change, Summary for Policymakers, IPCC (2013).
URL http://www.climatechange2013.org/

[2] International Energy Agency (IEA), Energy Technology Perspectives 2014, IEA, 2014. doi:10.1787/energy_tech-2014-en.

[3] O. Edenhofer, R. Pichs-Madruga, Y. Sokona, E. Farahani, S. Kadner, K. Seyboth, A. Adler, I. Baum, S. Brunner, P. Eickemeier, B. Kriemann, J. Savolainen, S. Schlømer, C. von Stechow, T. Zwickel, J. M. (eds.), Climate change 2014: Mitigation of climate change., Tech. rep., Working Group III Contribution to the Fifth Assessment Report of the Intergovernmental Panel on Climate Change, Summary for Policymakers, IPCC (2014).
URL http://mitigation2014.org/

[4] Norwegian Petroleum Directorate, Facts – the Norwegian petroleum sector (2014).
URL http://www.npd.no/en/Publications/Facts/Facts-2014/

[5] P. Aursand, M. Hammer, S. T. Munkejord, Ø. Wilhelmsen, Pipeline transport of CO_2 mixtures: Models for transient simulation, International Journal of Greenhouse Gas Control 15 (2013) 174–185. doi:10.1016/j.ijggc.2013.02.012.

[6] NETL, CO_2 impurity design parameters, Tech. Rep. DOE/NETL-341-011212, National Energy Technology Laboratory, USA (Aug. 2013).
URL http://www.netl.doe.gov/File%20Library/Research/Energy%20Analysis/Publications/QGESS_CO2Purity_Rev3_20130927_1.pdf

[7] H. Li, J. P. Jakobsen, Ø. Wilhelmsen, J. Yan, PVTxy properties of CO_2 mixtures relevant for CO_2 capture, transport and storage: Review of available experimental data and theoretical models, Applied Energy 88 (11) (2011) 3567–3579. doi:10.1016/j.apenergy.2011.03.052.

[8] H. Li, Ø. Wilhelmsen, Y. Lv, W. Wang, J. Yan, Viscosity, thermal conductivity and diffusion coefficients of CO_2 mixtures: Review of experimental data and theoretical models, International Journal of Greenhouse Gas Control 5 (5) (2011) 1119–1139. doi:10.1016/j.ijggc.2011.07.009.

[9] S. T. Munkejord, M. Hammer, S. W. Løvseth, CO_2 transport: Data and models – A review, Applied Energy 169 (2016) 499–523. doi:10.1016/j.apenergy.2016.01.100.

[10] H. Mahgerefteh, S. Brown, G. Denton, Modelling the impact of stream impurities on ductile fractures in CO_2 pipelines, Chemical Engineering Science 74 (2012) 200–210. doi:10.1016/j.ces.2012.02.037.

[11] D. G. Jones, A. Cosham, K. Armstrong, J. Barnett, R. Cooper, Fracture-propagation control in dense-phase CO_2 pipelines, in: 6th International Pipeline Technology Conference, Tiratsoo Technical, Ostend, Belgium, 2013, pp. 7–9, paper S06-02.

[12] A. Cosham, D. G. Jones, K. Armstrong, D. Allason, J. Barnett, Analysis of two dense phase carbon dioxide full-scale fracture propagation tests, in: International Pipeline Conference, IPC2014, Vol. 3, American Society of Mechanical Engineers, Calgary, Canada, 2014. doi:10.1115/IPC2014-33080.

[13] E. Aursand, C. Dørum, M. Hammer, A. Morin, S. T. Munkejord, H. O. Nordhagen, CO_2 pipeline integrity: Comparison of a coupled fluid-structure model and uncoupled two-curve methods, in: N. Røkke, H. Svendsen (Eds.), 7th Trondheim Conference on CO_2 Capture, Transport and Storage (TCCS-7), BIGCCS / SINTEF / NTNU, Energy Procedia, vol. 51, Trondheim, Norway, 2014, pp. 382–391. doi:10.1016/j.egypro.2014.07.045.

[14] DNV, Submarine pipeline systems, Offshore standard DNV-OS-F-101 (Aug. 2012).

[15] H. O. Nordhagen, S. Kragset, T. Berstad, A. Morin, C. Dørum, S. T. Munkejord, A new coupled fluid-structure modelling methodology for running ductile fracture, Computers & Structures 94–95 (2012) 13–21. doi:10.1016/j.compstruc.2012.01.004.

[16] B. N. Leis, X.-K. Zhu, T. P. Forte, E. B. Clark, Modeling running fracture in pipelines – Past, present, and plausible future directions, in: 11th International Conference on Fracture, ICF11, Vol. 8, 2005, pp. 5759–5764.

[17] M. Kanninen, P. O'Donoghue, Research challenges arising from current and potential applications of dynamic fracture mechanics to the integrity of engineering structures, International Journal of Solids and Structures 32 (17) (1995) 2423–2445. doi:10.1016/0020-7683(94)00275-2.

[18] X.-K. Zhu, Existing methods in ductile fracture propagation control for high-strength gas transmission pipelines, in: ASME Pressure Vessels and Piping Conference, Vol. 6B, American Society of Mechanical Engineers, Paris, France, 2013. doi:10.1115/PVP2013-98052.

[19] G. T. Hahn, M. Sarrate, M. F. Kanninen, A. R. Rosenfield, A model for unstable shear crack propagation in pipes containing gas pressure, International Journal of Fracture 9 (2) (1973) 209–222. doi:10.1007/BF00041863.

[20] W. A. Maxey, Fracture initiation, propagation and arrest, in: Fifth Symposium on Line Pipe Research, American Gas Association, Houston, Texas, USA, 1974, pp. J1–J31.

[21] R. Higuchi, H. Makino, I. Takeuchi, New concept and test method on running ductile fracture arrest for high pressure gas pipeline, in: 24th World Gas Conference, WGC 2009, Vol. 4, International Gas Union, Buenos Aires, Argentina, 2009, pp. 2730–2737.

[22] L. B. Freund, D. M. Parks, Analytical Interpretation of Running Ductile Fracture Experiments in Gas-pressurized pipelines, American Society for Testing and Materials, 1980, pp. 359–378. doi:10.1520/stp27457s.

[23] A. Arabei, I. Pyshmintsev, M. Shtremel, A. Glebov, A. Struin, A. Gervasev, Resistance of X80 steel to ductile-crack propagation in major gas lines, Steel in Translation 39 (9) (2009) 719–724. doi:10.3103/s0967091209090010.

[24] P. E. O'Donoghue, M. F. Kanninen, C. P. Leung, G. Demofonti, S. Venzi, The development and validation of a dynamic fracture propagation model for gas transmission pipelines, International Journal of Pressure Vessels and Piping 70 (1) (1997) 11–25. doi:10.1016/s0308-0161(96)00012-9.

[25] I. Scheider, A. Nonn, A. Völling, A. Mondry, C. Kalwa, A damage mechanics based evaluation of dynamic fracture resistance in gas pipelines, Procedia Materials Science 3 (0) (2014) 1956–1964. doi:10.1016/j.mspro.2014.06.315.

[26] T. Rabczuk, R. Gracie, J.-H. Song, T. Belytschko, Immersed particle method for fluid–structure interaction, International Journal for Numerical Methods in Engineering 81 (1) (2010) 48–71. doi:10.1002/nme.2670.

[27] H. Makino, T. Amano, Demonstration of crack arrestability of X100 line pipe and development of evaluation technologies for three-

dimensional fracture process, Tech. rep., Nippon Steel and Sumitomo Meta technocal report No. 107 (2015).
URL http://www.nssmc.com/en/tech/report/nssmc/pdf/107-07.pdf

[28] X. B. Yang, Z. Zhuang, X. C. You, Y. R. Feng, C. Y. Huo, C. J. Zhuang, Dynamic fracture study by an experiment/simulation method for rich gas transmission X80 steel pipelines, Engineering Fracture Mechanics 75 (18) (2008) 5018–5028. doi:10.1016/j.engfracmech.2008.06.032.

[29] G. Wilkowski, D.-J. Shim, Y. Hioe, S. Kalyanam, F. Brust, How new vintage line pipe steel fracture properties differ from old vintage line pipe steels, in: 9th International Pipeline Conference, IPC2012, ASME, Calgary, Canada, 2012. doi:10.1115/ipc2012-90518.

[30] G. Wilkowski, D. Rudland, H. Xu, N. Sanderson, Effect of grade on ductile fracture arrest criteria for gas pipelines, ASME Conference Proceedings 2006 (42630) (2006) 369–384. doi:10.1115/ipc2006-10350.

[31] A. Shterenlikht, S. H. Hashemi, I. C. Howard, J. R. Yates, R. M. Andrews, A specimen for studying the resistance to ductile crack propagation in pipes, Engineering Fracture Mechanics 71 (13) (2004) 1997–2013. doi:10.1016/j.engfracmech.2003.10.001.

[32] T. Berstad, C. Dørum, J. P. Jakobsen, S. Kragset, H. Li, H. Lund, A. Morin, S. T. Munkejord, M. J. Mølnvik, H. O. Nordhagen, E. Østby, CO_2 pipeline integrity: A new evaluation methodology, in: J. Gale, C. Hendriks, W. Turkenberg (Eds.), GHGT-10 – 10th International Conference on Greenhouse Gas Control Technologies, IEAGHGT, Energy Procedia vol. 4, Amsterdam, The Netherlands, 2011, pp. 3000–3007. doi:10.1016/j.egypro.2011.02.210.

[33] K. E. T. Giljarhus, S. T. Munkejord, G. Skaugen, Solution of the Span-Wagner equation of state using a density-energy state function for fluid-dynamic simulation of carbon dioxide, Industrial & Engineering Chemistry Research 51 (2) (2012) 1006–1014. doi:10.1021/ie201748a.

[34] M. Hammer, Å. Ervik, S. T. Munkejord, Method using a density-energy state function with a reference equation of state for fluid-dynamics simulation of vapor-liquid-solid carbon dioxide, Industrial & Engineering Chemistry Research 52 (29) (2013) 9965–9978. doi:10.1021/ie303516m.

[35] E. Aursand, P. Aursand, T. Berstad, C. Dørum, M. Hammer, S. T. Munkejord, H. O. Nordhagen, CO_2 pipeline integrity: A coupled fluid-structure model using a reference equation of state for CO_2, in: T. Dixon, K. Yamaji (Eds.), GHGT-11 – 11th International Conference on Greenhouse Gas Control Technologies, RITE / IEAGHGT, Energy Procedia, vol. 37, Kyoto, Japan, 2013, pp. 3113–3122. doi:10.1016/j.egypro.2013.06.197.

[36] A. Cosham, D. G. Jones, K. Armstrong, D. Allason, J. Barnett, Ruptures in gas pipelines, liquid pipelines and dense phase carbon dioxide pipelines, in: 2012 9th International Pipeline Conference, American Society of Mechanical Engineers, 2012, pp. 465–482. doi:10.1115/ipc2012-90463.

[37] DNV, Design and operation of CO_2 pipelines, Recommended Practice DNV-RP-J202 (Apr. 2010).

[38] S. Røneid, T. Bubenik, Fracture arrest testing of CO_2 pipelines, in: Offshore Pipeline Technology Conference, Amsterdam, The Netherlands, 2014.

[39] J. O. Hallquist, LS-DYNA Keyword User's Manual, Livermore Software Technology Corporation (2007).

[40] M. G. Cockcroft, D. J. Latham, Ductility and the workability of metals, Journal of the Institute of Metals 96 (1968) 33–39.

[41] K. G. Rakvåg, T. Børvik, O. S. Hopperstad, A numerical study on the deformation and fracture modes of steel projectiles during taylor bar impact tests, International Journal of Solids and Structures 51 (3) (2014) 808–821. doi:10.1016/j.ijsolstr.2013.11.008.

[42] J. K. Holmen, O. S. Hopperstad, T. Børvik, Low-velocity impact on multi-layered dual-phase steel plates, International Journal of Impact Engineering 78 (2015) 161–177. doi:10.1016/j.ijimpeng.2014.12.005.

[43] E. Voce, The relationship between stress and strain for homogeneous deformation, Journal of the Institute of Metals 74 (1948) 537–562.

[44] J. Besson, Continuum models of ductile fracture: A review, International Journal of Damage Mechanics 19 (1) (2009) 3–52. doi:10.1177/1056789509103482.

[45] L. Xue, T. Wierzbicki, Numerical simulation of fracture mode transition in ductile plates, International Journal of Solids and Structures 46 (6) (2009) 1423–1435. doi:10.1016/j.ijsolstr.2008.11.009.

[46] T. F. Morgeneyer, T. Taillandier-Thomas, L. Helfen, T. Baumbach, I. Sinclair, S. Roux, F. Hild, In situ 3-D observation of early strain localization during failure of thin Al alloy (2198) sheet, Acta Materialia 69 (2014) 78–91. doi:10.1016/j.actamat.2014.01.033.

[47] C. Tekoğlu, J. W. Hutchinson, T. Pardoen, On localization and void coalescence as a precursor to ductile fracture, Philosophical Transactions of the Royal Society of London A: Mathematical, Physical and Engineering Sciences 373 (2038) (2015), Article 20140121. doi:10.1098/rsta.2014.0121.

[48] K. L. Nielsen, J. W. Hutchinson, Cohesive traction-separation laws for tearing of ductile metal plates, International Journal of Impact Engineering 48 (SI) (2011) 15–23. doi:10.1016/j.ijimpeng.2011.02.009.

[49] T. Børvik, S. Dey, A. H. Clausen, Perforation resistance of five different high-strength steel plates subjected to small-arms projectiles, International Journal of Impact Engineering 36 (7) (2009) 948–964. doi:10.1016/j.ijimpeng.2008.12.003.

[50] T. Børvik, O. S. Hopperstad, K. O. Pedersen, Quasi-brittle fracture during structural impact of AA7075-T651 aluminium plates, International Journal of Impact Engineering 37 (2010) 537–551. doi:10.1016/j.ijimpeng.2009.11.001.

[51] M. Kristoffersen, T. Børvik, I. Westermann, M. Langseth, O. S. Hopperstad, Impact against X65 steel pipes – an experimental investigation, International Journal of Solids and Structures 50 (20-21) (2013) 3430–3445. doi:10.1016/j.ijsolstr.2013.06.013.

[52] H. Nordhagen, S. Dumoulin, G. Gruben, Main properties governing the ductile fracture velocity in pipelines: A numerical study using an (artificial fluid)-structure interaction model, Procedia Materials Science 3 (2014) 1650–1655. doi:10.1016/j.mspro.2014.06.266.

[53] N. Stander, W. Roux, T. Goel, T. Eggleston, K. Craig, LS-OPT User Manual Version 4.1, Livermore Software Technology Corporation (2010).

[54] A. Rusinek, J. A. Rodríguez-Martínez, J. R. Klepaczko, R. B. Pęcherski, Analysis of thermo-visco-plastic behaviour of six high strength steels, Materials & Design 30 (5) (2009) 1748–1761. doi:10.1016/j.matdes.2008.07.034.

[55] G. R. Johnson, W. H. Cook, A constitutive model and data for metals subjected to large strains, high strain rates and high temperatures, in: Proceedings of the 7th International Symposium on Ballistics, Vol. 21, The Netherlands, 1983, pp. 541–547.

[56] P. Nègre, D. Steglich, W. Brocks, Crack extension at an interface: prediction of fracture toughness and simulation of crack path deviation, International Journal of Fracture 134 (3-4) (2005) 209–229. doi:10.1007/s10704-005-0523-8.

[57] R. Span, W. Wagner, A new equation of state for carbon dioxide covering the fluid region from the triple-point temperature to 1100 K at

pressures up to 800 MPa, Journal of Physical and Chemical Reference Data 25 (6) (1996) 1509–1596. `doi:10.1063/1.555991`.

[58] S. T. Munkejord, M. Hammer, Depressurization of CO_2-rich mixtures in pipes: Two-phase flow modelling and comparison with experiments, International Journal of Greenhouse Gas Control 37 (2015) 398–411. `doi:10.1016/j.ijggc.2015.03.029`.

[59] E. F. Toro, MUSTA: A multi-stage numerical flux, Applied Numerical Mathematics 56 (10-11) (2006) 1464–1479. `doi:10.1016/j.apnum.2006.03.022`.

[60] S. T. Munkejord, S. Evje, T. Flåtten, The multi-stage centred-scheme approach applied to a drift-flux two-phase flow model, International Journal for Numerical Methods in Fluids 52 (6) (2006) 679–705. `doi:10.1002/fld.1200`.

[61] G. Hou, J. Wang, A. Layton, Numerical methods for fluid-structure interaction: a review, Communications in Computational Physics 12 (2) (2012) 337–377. `doi:10.4208/cicp.291210.290411s`.

[62] K. D. Ives, A. K. Shoemaker, R. F. McCartney, Pipe deformation during a running shear fracture in line pipe, Journal of engineering materials and technology 96 (4) (1974) 309–317. `doi:10.1115/1.3443246`.

[63] D.-J. Shim, G. Wilkowski, D. Rudland, B. Rothwell, J. Merritt, Numerical simulation of dynamic ductile fracture propagation using cohesive zone modeling, in: 2008 7th International Pipeline Conference, American Society of Mechanical Engineers, 2008, pp. 21–28. `doi:10.1115/ipc2008-64049`.

[64] G. Berardo, P. Salvini, G. Mannucci, G. Demofonti, On longitudinal propagation of a ductile fracture in a buried gas pipeline: numerical and experimental analysis, in: Proceedings of the 2000 International Pipeline Conference, Vol. 1, 2000, pp. 287–294.

[65] A. Volling, M. Erdelen-Peppler, C. Kalwa, H. Brauer, B. Ouaissa, H. Meuser, Numerical approach for crack-arrest prediction by FEM, in: 6th International Pipeline Technology Conference, 2013, pp. S19–01.

[66] D. Rudland, G. Wilkowski, Effects of backfill soil properties and pipe grade on ductile fracture arrest, in: Proceedings of the 16th Biennial PRCI/EPRG/APIA Joint Technical Meeting on Pipeline Research, 2007, pp. 16–19.

[67] D. Rudland, G. Wilkowski, B. Rothwell, The effects of soil properties on the fracture speeds of propagating axial cracks in line pipe steels, in: 6th Biennial International Pipeline Conference, IPC, Vol. 3 PART A, ASME, Calgary, Canada, 2006, pp. 73–82. `doi:10.1115/IPC2006-10086`.

[68] G. Demofonti, A. Maresca, G. Buzzichelli, Ductile fracture propagation and arrest in offshore pipelines, Applied Mechanics Reviews 41 (2) (1988) 85–95. `doi:10.1115/1.3151883`.

[69] W. A. Maxey, Final report on gas expansion studies: to American Gas Association, Tech. Rep. NG-18 Report No. 133, Battelle Columbus Laboratories (1983).

[70] D. Rudland, D. Shim, H. Xu, D. Rider, P. Mincer, D. Shoemaker, G. Wilkowski, First major improvements to the two-curve ductile fracture model, Tech. Rep. Emc2 Report to US DOT and PRCI, PRCI (2007).

[71] P. Salvini, G. Berardo, G. Demofonti, G. Mannucci, Numerical model of the backfill constraint effect during fracture propagation on buried large diameter gas pipelines, in: Proceedings of Pipeline Technology Conference PTC2000, Vol. 1, 2000, pp. 21–24.

[72] B. Cotterell, J. R. Rice, Slightly curved or kinked cracks, International Journal of Fracture 16 (2) (1980) 155–169. `doi:10.1007/bf00012619`.

[73] J. J. Monaghan, Smoothed particle hydrodynamics, Reports on Progress in Physics 68 (8) (2005) 1703–1759. `doi:10.1088/0034-4885/68/8/r01`.

[74] C. Lu, G. Michal, P. Venton, A new fracture velocity model for high grade gas pipelines, in: 20th Joint Technical Meeting on Pipeline Research, 2015.

[75] G. M. Wilkowski, W. A. Maxey, R. J. Eiber, Use of a brittle notch DWTT specimen to predict fracture characteristics of line pipe steels, in: ASME 1977 Energy Technology Conference, Houston, Texas, Paper, 1977, pp. 18–22.

[76] T. Anderson, Fracture Mechanics, Fundamentals and Applications, 3rd Edition, CRC Press, 2005.

[77] E. Sugie, M. Matsuoka, H. Akiyama, T. Mimura, Y. Kawaguchi, A study of shear crack-propagation in gas-pressurized pipelines, Journal of Pressure Vessel Technology – Transactions of the ASME 104 (4) (1982) 338–343. `doi:10.1115/1.3264226`.

[78] H. Makino, T. Inoue, S. Endo, T. Kubo, T. Matsumoto, Simulation method for shear fracture propagation in natural gas transmission pipelines, International Journal of Offshore and Polar Engineering 14 (1) (2004) 60–68.